ACTIVE MULTISPECTRAL BIDIRECTIONAL DISTRIBUTION FUNCTION MEASUREMENT SYSTEM

THESIS

Mark J. Proctor, Captain, USAF

AFIT/GEO/ENG/00M-02

DEPARTMENT OF THE AIR FORCE
AIR UNIVERSITY

AIR FORCE INSTITUTE OF TECHNOLOGY

Wright-Patterson Air Force Base, Ohio

APPROVED FOR PUBLIC RELEASE; DISTRIBUTION UNLIMITED.

The views expressed in this thesis are those of the author and do not reflect the official policy or position of the Department of Defense or the United States Government.

20000815 174

ACTIVE MULTISPECTRAL BIDIRECTIONAL
REFLECTANCE DISTRIBUTION
FUNCTION MEASUREMENT SYSTEM

THESIS

Presented to the Faculty

Department of Systems and Engineering Management

Graduate School of Engineering and Management

Air Force Institute of Technology

Air University

Air Education and Training Command

In Partial Fulfillment of the Requirements for the

Master of Science in Electrical Engineering

Mark J. Proctor, B.S.

Captain, USAF

March 2000

AFIT/GEO/ENG/00M-02

ACTIVE MULTISPECTRAL BIDIRECTIONAL
REFLECTANCE DISTRIBUTION
FUNCTION MEASUREMENT SYSTEM

Mark J. Proctor, B.S.E.E.
Captain, USAF

Approved:

_____

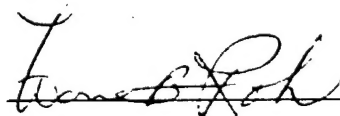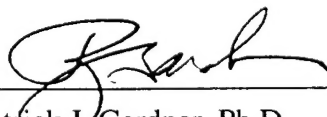Eric P. Magee, Ph.D.
Chairman, Advisory Committee

3 MAR 2000
_____
Date

_____

Won B. Roh, Ph.D.
Member, Advisory Committee

3 Mar 00
_____
Date

_____

Patrick J. Gardner, Ph.D.
Member, Advisory Committee

16 Feb 00
_____
Date

Acknowledgements

This research could not have been accomplished without the help of many people. I would like to begin by thanking each of my committee members: my advisor Maj Magee, Dr. Roh, and Maj Gardner. Your support was instrumental in the process of developing a truly worthwhile and useful BRDF measurement system which should be greatly beneficial to the Unites States military establishment. I would also like to thank Capt Brad Rennich for providing and supporting this research opportunity with both equipment and extensive technical expertise.

A special thanks must go out to my wife, Michelle (*Meche*), who has been extremely supportive during the past 16 months of my mental absence. Without your encouragement and continual quest for knowledge, entering and completing this program would not have become a reality.

Mark J. Proctor

Table of Contents

List of Figures

List of Tables

Abstract

Today's highly technical battlefield environment dictates the need for a method of standoff target identification, which reduces risk to personnel and equipment. It is widely known that a given material will react differently to incident radiation than a dissimilar material. Certain materials may respond specularly while others tend to be diffuse. By measuring these responses, materials can be identified by comparison with a known database.

One method of building such a database for target recognition is by employing an active multispectral bidirectional reflectance distribution function (BRDF) measurement system. In the following text, such a system is developed and tested using a 1.5μm - 1.7μm and 2.0μm - 2.4μm tunable source. The system does not yet meet the desired 1.0μm - 5.0μm range; however, all major system components with exception to the source are well suited for this entire band. A detailed description of the components used is presented along with recommendations for further research.

This particular BRDF measurement system implementation is the direct result of a previous attempt that encountered numerous errors. These errors were primarily attributable to nonlinearities, attenuation, and misalignments in the equipment utilized. Considerable effort was expended in order to reduce these anomalies mainly through component replacement. A comprehensive error analysis is presented for this system

along with recommendations for a new system, which should reduce these abnormalities

and improve data integrity and collection efficiency.

ACTIVE MULTISPECTRAL BIDIRECTIONAL REFLECTANCE DISTRIBUTION FUNCTION MEASUREMENT SYSTEM

I. Introduction

Optical scatter has long been regarded as nothing more than an inconvenient source of optical noise. It leads to image distortion and limits power throughput; however, optical scatter can be used to characterize optical component quality. More relevant to this research is the fact that it is also used to identify material properties such as roughness, position, orientation, and homogeneity.

Materials respond differently to incident radiation due to varying surface and atomic properties. Identification is made possible through the measurement of reflected or emitted radiation; however, it is possible to incorrectly identify a material in a monochromatic system. Certain materials will respond specularly to a given radiation wavelength, while others yield a diffuse or Lambertian response; most materials exhibit combinations of both. This uncertainty in identification creates the need for a multispectral system.

A multispectral system can be used to monitor the reflected or emitted radiation over varying spectral bands; such a system can either be passive or active. A passive system relies upon radiation which is emitted directly from the material or reflected by the material from some external source not part of the measurement system. Self-emitted radiation is typically above the mid-wave infrared (MWIR) 3μm - 5μm band, which is referred to as the thermal infrared. Reflected radiation is typically the result of visible

1

through short-wave infrared (SWIR) solar radiation (0.4µm - 3µm). The MWIR band is considered a transition region between the solar-reflected and thermal infrared bands.

Unfortunately, passive multispectral systems have limitations such as a reliance upon naturally emitted radiation or the presence of solar radiation for reflective measurements. Many materials of interest do not self-emit; therefore, a passive system may be restricted to measuring solar reflection. This, of course, may not be possible during low or no light situations. A solution to this problem is the active multispectral system.

Active systems have been fielded for some time in both LIDAR (light detection and ranging) and LADAR (laser detection and ranging) forms. These systems were designed to determine target range and direction by measuring the round-trip distance for a given radiated pulse. Since these systems measure reflected radiation, they are highly dependent upon the reflective nature of the target. This leads to the extension of LADAR system capabilities by measuring incident and reflected radiation levels in order to resolve target identification.

Unfortunately, active multispectral systems are more easily designed than developed. In order to match the theoretical capabilities of the passive multispectral system, an active system must be able to produce light nearly continuously across a relatively large spectrum. This means that the source must be tunable or composed of multiple sources capable of producing each of the desired wavelengths. The latter is impractical from an experimental viewpoint and less so in an operational environment, leaving tunable sources as a singular feasible option.

Tunable lasers are not a novel concept, nor are they necessarily complicated in design. However, difficulties arise in developing a laser that is widely tunable. In the case of optical parametric oscillators (OPO), the transparency region of the tuning nonlinear crystal and the pump wavelength limit the tunable range. Such limitations create the need for highly precise and accurate measurements across a large band, which can later be optimized to reduce the range necessary for target identification in an operational environment.

1.1 Problem Statement and Scope

Target identification is necessary in order to differentiate friend from foe and vehicle type. Systems, such as Identify Friend or Foe (IFF), are already in existence; however, these transponders are typically limited to aircraft and are seldom in use during clandestine activities. Furthermore, identification of ground targets is generally left to the observer's naked eye through analysis of intelligence images or a direct visual. Each of these methods can lead to unnecessary casualties for both enemy and allied forces. This leads to the development of standoff target identification systems similar to the active multispectral system described in this document.

This particular system measures the bidirectional reflectance distribution function (BRDF), which is a subset of the bidirectional scatter distribution function (BSDF). These measurements are dependent upon wavelength and orientation, but are independent of the system used to record the measurements. Consequently, these results are repeatable and useful in material identification, which can lead to target identification.

1.2 Contributions

The research described in this document has lead to key contributions in the fields of material classification, band selection optimization, and target recognition. By running a pre-existing correlation band (CBand) selection algorithm against normalized class reflectances, an optimal class band-pair can be determined [19]. This can effectively reduce the number of discrete sources or the necessary range of a tunable source for target identification. This research is intended to produce a sufficient amount of spectral data that may be later used to determine the optimal band-pair for a given target.

1.3 Thesis Organization

This thesis is organized into four chapters. Chapter II provides background information on the BRDF and scatter theory. Chapter III presents the recommended optimized monostatic BRDF measurement system along with the monostatic system used in this research including a complete component breakdown [19]. Chapter IV offers and analyzes the BRDF data collected by this system and a modified bistatic version and discusses potential sources of error. Further improved monostatic and bistatic BRDF measurement system designs are also presented in Chapter V. The new configurations are intended to improve the integrity of the data collected by reducing errors and uncertainties in the equipment used. Chapter V also provides a summary of the findings in this study and offers insight into additional research.

II. BRDF Measurement

2.1 Overview

Optical scatter has long been regarded as an inconvenient source of optical noise, which leads to image distortion and limits power throughput. Conversely, it is deemed to be a highly sensitive metrology tool. Moreover, the significance of optical scatter is no longer limited to the optics community. Other industries are now using this material property to define others such as surface roughness, homogeneity, and orientation.

The bidirectional scatter distribution function (BSDF) is now regarded as the universal method for expressing scatter data. Scatter from optical components or materials can propagate in all directions within the observation sphere centered about the sample of interest. The pattern with which this scattered light disseminates is a function of wavelength, angle of incident radiation, and sample properties. Material properties, which affect the distribution of scattered energy, include reflectance, transmittance, emissivity, texture, purity, index of refraction, etc. Furthermore, these properties may differ between the surface and bulk (or core) of the material.

The BSDF, as previously mentioned, is a commonly used format for expressing scatter data in all forms. However, this data can be broken into smaller subsets of the BSDF referred to as the BRDF, BTDF, and BVDF. These are used specifically for reflective, transmissive, and volume scatter sources, respectively [26].

The Air Force Research Laboratory (AFRL) has a requirement for a BRDF measurement system capable of producing curves at discrete wavelengths from 1.5μm to 5.0μm [19]. The measurement system described in this document is designed to provide

5

BRDF measurements between 1.5μm - 1.7μm and 2.0μm - 2.4μm. This limitation is strictly source related and, with current advancements in optical parametric oscillator (OPO) technology, removal of these constraints is in the foreseeable future and should fulfill the stated requirements.

The BRDF data included was collected at the Air Force Institute of Technology's (AFIT) Electrical Engineering Department laboratory in building 194, Wright-Patterson AFB, OH. The equipment necessary to construct the measurement system described in this text was subject to availability. Therefore, recommended modifications are presented in Chapter V.

Since the BRDF is such a universally accepted term used to describe reflected scattered light, it is worthwhile to understand its mathematical and geometrical definitions along with its variations and limitations. Therefore, this chapter addresses the BRDF and material properties that are responsible for scatter. This is followed by a detailed description of a monostatic and bistatic measurement system used in this research to obtain BRDF data. Additionally, experimental data is presented with a comparative analysis against known reflectance standards. A statistical analysis of errors and possible error sources is then provided and succeeded by recommended improvements to both systems for future research.

2.2 Background

The BRDF is a unit of measure for the reflective properties of a material. It is functionally dependent upon the wavelength of incident light, illumination geometry, and viewing geometry. It is also determined by the structural and optical properties of the

surface and bulk of the material such as transmission, reflection, absorption, emission, and homogeneity. BRDF is defined in radiometric terms as the scattered surface radiance ($Wm^{-2}sr^{-1}$) at some point on the hemisphere in front of the reflective sample, divided by the incident surface irradiance (Wm^{-2}). It is denoted as ρ' and carries units of sr^{-1} [26]. The BRDF is mathematically defined below:

$$\rho'(\theta_i,\phi_i,\theta_r,\phi_r;\lambda) = \frac{dL(\theta_r,\phi_r;\lambda)}{dL(\theta_i,\phi_i;\lambda)\cos\theta_i\, d\omega_i} \qquad (1)$$

where dL is the differential radiance, θ_i and ϕ_i are the zenith and azimuth incident angles, and θ_r and ϕ_r are the zenith and azimuth reflected angles. The differential incident beam solid angle, $d\omega_i$, is a combination of the differential incident beam to zenith angle, $d\theta_i$, and the differential incident beam azimuth angle, $d\phi_i$. Refer to Appendix C for additional methods of computing the BRDF.

This method may be simplified by assuming the incident beam of light to be collimated with uniform cross-section. Additional simplification can be made by assuming the illuminated area of the sample to be isotropic (i.e. physical properties are independent of direction) and further presuming that all scattered radiation originates from the surface of the material and not from the bulk. With these assumptions, Equation (1) reduces to [26]

$$\rho' = \frac{differential\, radiance}{differential\, irradiance} \cong \frac{dP_r/d\Omega_r}{P_i\cos\theta_r} \cong \frac{P_r/\Omega_r}{P_i\cos\theta_r} \qquad (2)$$

where P_r is the measured power reflected from the sample and Ω_r is the solid angle, subtended by the measurement device, through which P_r is scattered. P_i is the total power
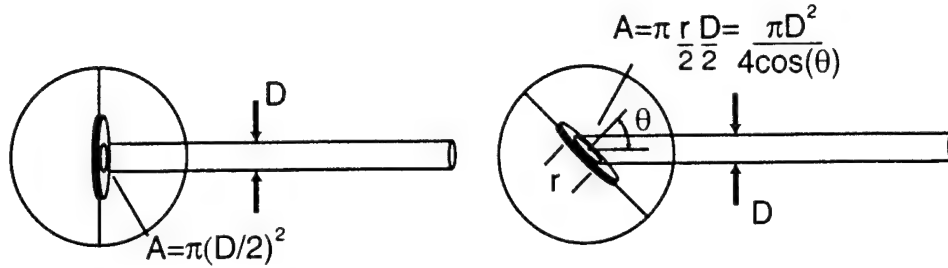
Figure 1 – Radiance as a Function of Angle of Incidence

incident upon the sample and $\cos(\theta_r)$ is a correction factor. In the case of directional

hemispherical reflectance (DHR) measurements where the angle of incidence is typically

fixed, this factor adjusts the sample's illuminated area to its apparent size when viewed

from the scatter direction. For monostatic BRDF measurements, the illuminated target

area, as viewed from the target detector, does not change. However, the radiance at the

target becomes a function of θ_r due to the increase in area illuminated by the incident beam

as the target is rotated in either direction from 0° (refer to Figure 1). Consequently,

radiance falls off with the $\cos(\theta_r)$ term causing the intensity (measured in Wsr^{-1}) and power

measured at the detector to follow suit.

The angle, θ_r, is measured between the incident radiation axis and the sample

surface normal. A geometrical representation of the BRDF is shown in Figure 2. The

"bidirectional" in BRDF refers to the fact that it is dependent upon both the incident and

scattered directions of propagation. Therefore, a truly accurate depiction of this function

includes a source that is capable of interrogating the sample from all angles within its

hemisphere. The scatter measurement device must also be capable of being placed at any

location within this same hemisphere. However, the incident radiation and scatter

measurement can be fixed in plane by applying the assumptions previously mentioned.

8
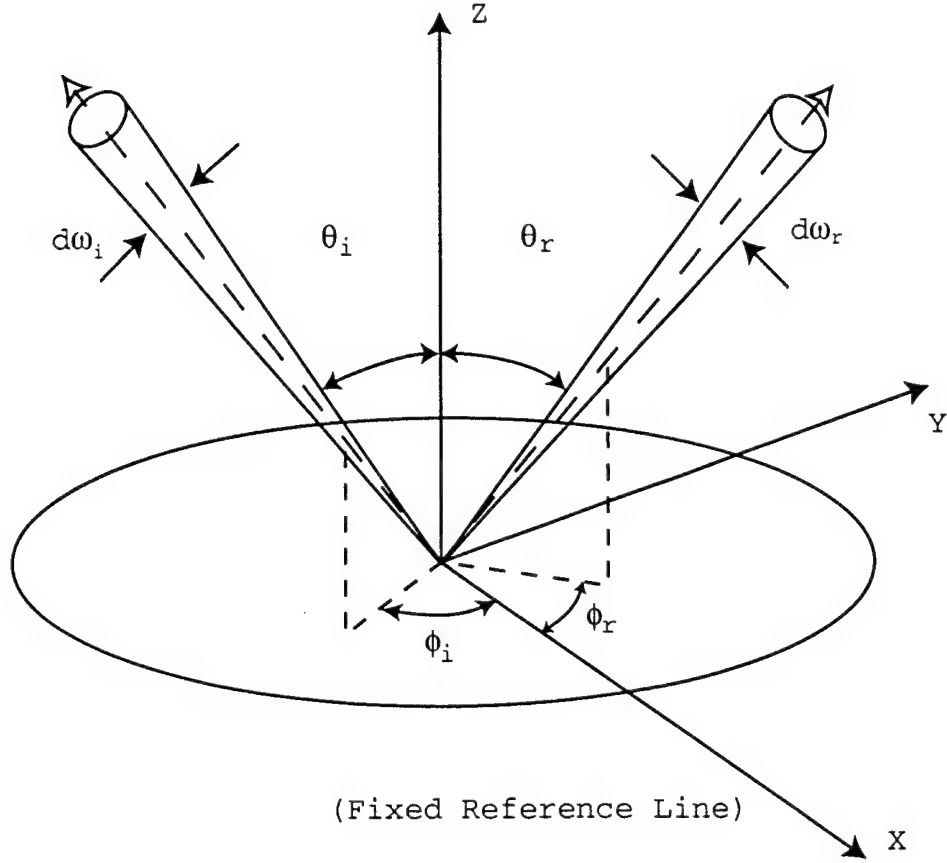
Figure 2 - Geometrical Representation of BRDF [15]

Refer to Figure 3 for a simplified geometrical representation of BRDF in bistatic and monostatic forms.

Some concern arises over the fact that the BRDF can vary so profusely. Referring to Equation (2), the ratio (P_r/P_i) becomes nearly unity when a specular reflection is encountered; this leads to a maximum BRDF of $1/\Omega_r$. Since these solid angles tend to be limited by finite apertures, the BRDF is likely to be relatively large[1]. Conversely, diffuse scatter can lead to extremely low levels of reflected radiation and BRDF values. This may present difficulties when selecting a measurement device, since smaller values of P_r

---

[1] Finite detector apertures allow for the reduction of the BRDF from differential (dP_r/dP_i) to absolute form (P_r/P_i) [26].

9
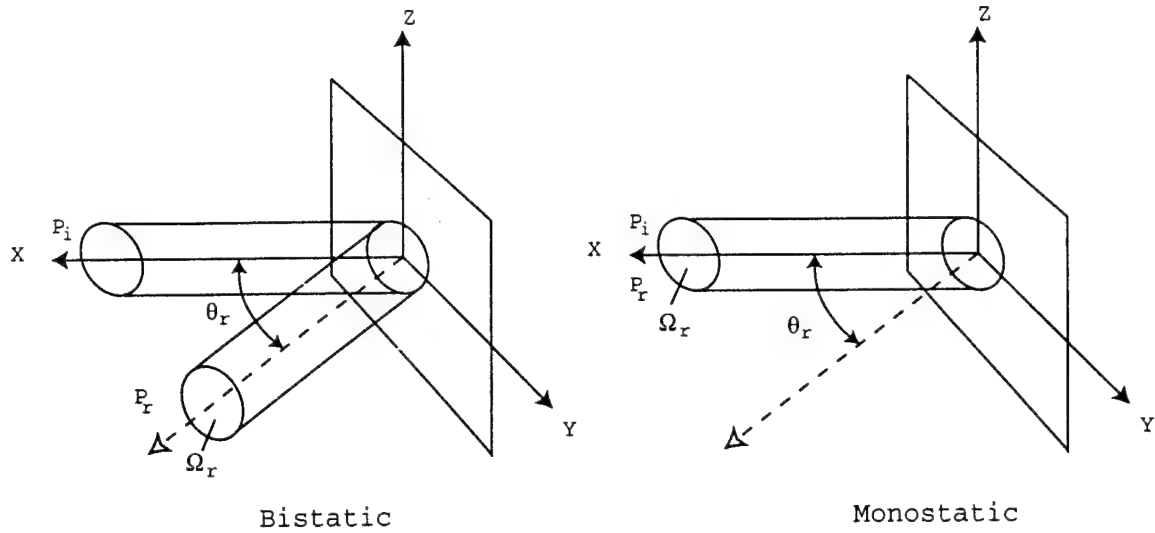
Figure 3 - Simplified BRDF Geometry for Bistatic and Monostatic Cases

require larger detector apertures. Even greater difficulty arises when attempting to satisfy

both conditions in a given measurement system.

Limiting measurements in plane using the bistatic or monostatic methods

significantly reduces sample characterization time. Additionally, out-of-plane

measurements will not contribute to the characterization of a target sample if the sample

surface is truly uniform or isotropic. One method of reducing or removing any

uncertainties regarding surface uniformity is to rotate the sample about the axis defined by

the target surface normal and at a sufficient rate allowing any variations to be averaged

out. Another potential source of error, which warrants discussion, is called *speckle effect*.

2.3 Speckle Effect

Imaging by coherent light leads to diffraction patterns such as Airy spots or

speckle. Often such patterns are prejudicial to the quality of imaging. Incoherent light

cancels these patterns by averaging and can indeed be considered as a superposition of a very large number of coherent components, whose phase factors are distributed at random [20].

Speckle diameter for a monochromatic source is defined by

$$S = \frac{\lambda z}{D}$$

(3)

where, in this case, λ is wavelength of the light incident upon and reflected by the target, z is the distance that the reflected light travels between the target and the target detector, and D is the diameter of the spot on the target [11]. From this simple equation, methods for reducing speckle are obvious. Assuming the source to be monochromatic, the distance between the target and target detector can be reduced and the spot size of the beam on the target can be increased in order to decrease the average speckle size. By decreasing the speckle size, the number of speckle incident upon the active area of the detector will increase causing a reduction in speckle effect by averaging out any time or spatial variations. For example, decreasing z and, consequently, the speckle size by 50% decreases the area of the speckle by 75%. This 75% decrease in speckle size area results in a 300% increase in the amount of speckle collected by a given detector.

2.4 Rayleigh, Topographic, Material, and Defect Scattering

When photons encounter particles, each molecule within the particle acts as an oscillator whose electron cloud can be driven into a ground-state vibration by an incoming photon [14]. This vibration induces the re-emission of another photon at the same

11

wavelength in all directions due to the random orientation of the molecules. Small particles (1/10th the wavelength of the incident light) tend to symmetrically scatter the photons with greater concentrations in the forward and aft directions. Large particles (0.25λ) scatter symmetrically with primary concentration in the forward direction while even larger particles (>λ) increasingly scatter into the forward direction. However, particles larger than the incident light wavelength tend to develop multiple maxima and minima at wider angles [25].

Surface roughness is another source of optical scatter. In fact, *topographic scatter* is the principle source of scattering from most optical surfaces at visible wavelengths [5]. The *topographic scatter* manifests itself in the form of phase fluctuations in the reflected wavefront resultant from surface height deviations. Another type of *material scatter* is the product of fluctuations in the composition or density of a material surface. These may cause scatter regardless of the smoothness of the surface.

Material and *topographic scatter* assume the perturbations responsible for scatter to be distributed broadly and continuously across the material surface. This is not the case for *defect scatter*, which is caused by localized aberrations such as pits, bumps, or patches of varying reflectivities.

III. BRDF System Configuration

BRDF measurement systems exist in many forms. These systems may or may not be restricted to measurements in the plane-of-incidence. In planar systems the light source and the target surface normal define the plane in which measurements will be taken. Here the target detector, which is used to measure reflected power from the target sample, is restricted to this plane. In a non-planar system the target detector is no longer restricted and may be used to take measurements throughout the entire hemisphere or sphere. These systems may also take a monostatic or bistatic approach to measuring reflected data. In a monostatic system the light source propagation axis and the target receiver are co-boresighted. This is accomplished by placing a beamsplitter just before the target with an orientation such that a portion of the reflected power is diverted onto the target detector.

The system shown in Figure 4 displays the optimized monostatic plane-of-incidence measurement system recommended for this research [19]. However, modifications were necessary due to equipment availability. The actual monostatic system implemented is shown in Figure 5. A modified bistatic version will be discussed later.

3.1 Source

As mentioned earlier, AFRL has a requirement for a BRDF measurement system capable of producing BRDF curves at discrete wavelengths from 1.5μm and 5.0μm [19]. However, source limitations restricted the range to 1.5μm - 1.7μm and 2.0μm - 2.4μm.
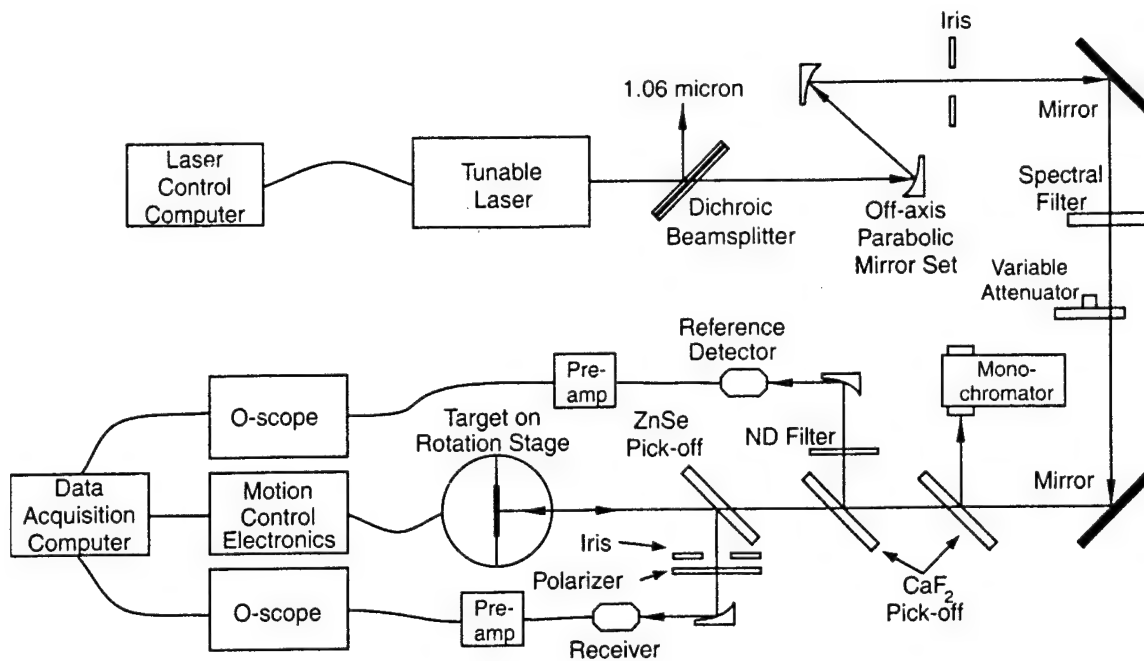
Figure 4 – Recommended Monostatic BRDF Measurement System [19]

The source used in this experiment is a tunable range imaging LADAR system developed by Q-Peak, Inc (see Section 4.2.1). The core technology of this system is a 10 kHz acousto-optically modulated diode-laser-pumped 1.046μm Nd:YLF laser that is frequency doubled to 523μm in order to pump a titanium-doped-sapphire (Ti:S) laser [3]. The output of the Ti:S cavity is then tuned by means of a computer controlled mechanically adjustable birefringent filter which is located within the cavity. The tuned output from the Ti:S cavity is then used to pump a rubidium-titanyl-arsenate (RTA) optical parametric oscillator (OPO) cavity which produces the 1.5μm - 1.7μm signal beam and the 2.0μm - 2.4μm idler beam. These ranges are achieved by tuning the Ti:S pump within its 0.59μm - 0.62μm band.
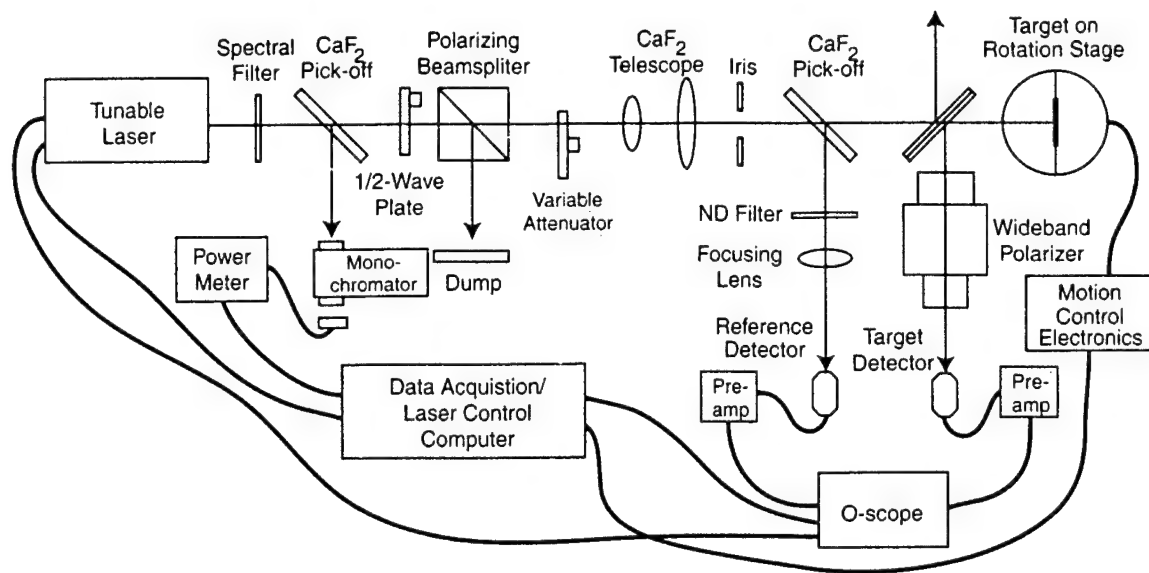
Figure 5 - Actual Monostatic BRDF Measurement System

By q-switching the Nd:YLF, the system is able to produce a peak intensity many times the CW level with a maximum of 6 kW peak power vs. 300mW average. This is accomplished by delaying the q-switch pulse until the gain medium reaches maximum population inversion (or the inversion ratio n_i/n_{th} is maximized) [30]. The pulse is also used to externally trigger the oscilloscope.

3.2 Optical Components

In order to remove the signal or idler beam and any pump leakage, a spectral filter is placed immediately downstream from the source. An interchangeable bandpass filter was chosen to pass the signal beam and a lowpass filter was selected to pass the idler beam. The filtered output is then transmitted through a CaF_2 pickoff oriented at 45° to the propagation axis, which reflects a portion of the beam into a computer controlled scanning monochromator. The CaF_2 substrate was chosen because of its 0.13μm - 10.0μm and relatively flat (90% - 95%) transmission range [2]. The refractive index of 1.399 at 5μm

15

corresponds to a Brewster's angle of 54°, which allows the pickoff to be oriented at 45° without excessive attenuation of the reflected portion of the p-polarized input beam.

The monochromator, which contains the necessary grating to scan the desired wavelength range, is a pass through system. Consequently, a thermal power detector is placed at the output of the monochromator in order to detect the selected wavelength. Both the power meter and monochromator base control units are capable of being controlled remotely via computer allowing for integration into the data acquisition and control computer system.

The beam transmitted through the CaF_2 pickoff is then sent through a ½-wave plate and polarizing beamsplitter, which collectively select the desired input linear polarization (see Section 4.2.2). Next, a variable neutral density filter is used to attenuate the signal. This component increases the range of targets for which the system can effectively collect data by allowing a reduced incident power for specular targets and increased power for diffuse targets without system recharacterization. After attenuation, the beam is expanded and collimated using a CaF_2 telescope (refer to Section 4.2.3). An iris placed at the target side of the telescope then selects a relatively uniform portion of the expanded beam. It also serves to prevent clipping and subsequent scatter by downstream components. The sampled beam is then reflected into the reference detector branch using another CaF_2 pickoff oriented at 45°. The reflectance properties for the CaF_2 substrate used in this configuration are shown in Figure 6. These results are based on experimental index of refraction measurements [9].
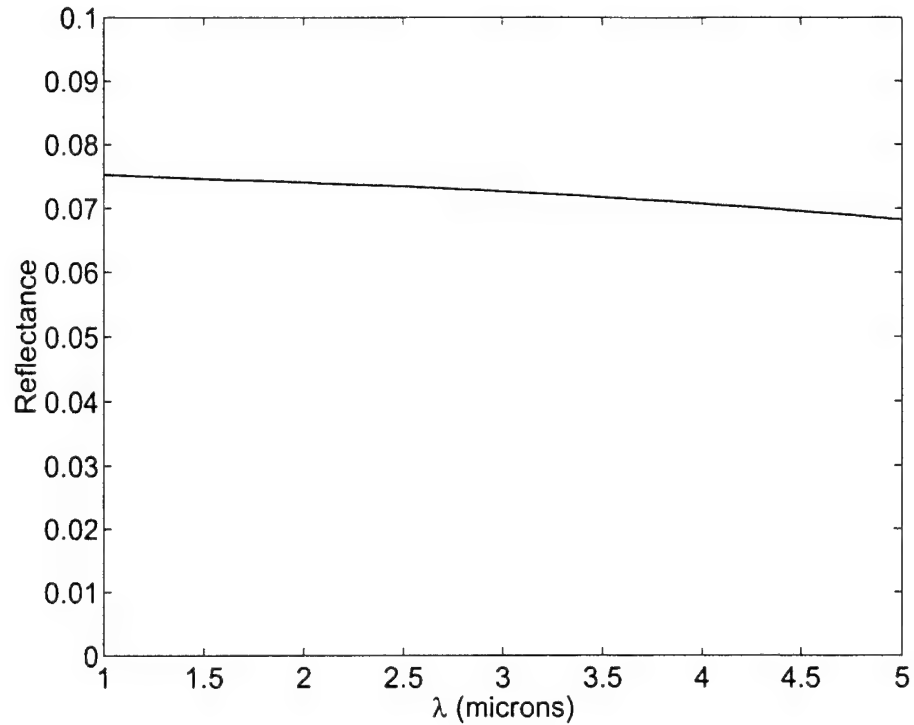
Figure 6 - S-Polarized Fresnel Reflectance from a Calcium Fluoride Window at 45°

Due to the inability to confirm the true orientation of the pickoff and the uncertainties associated with source polarization, data was collected in an effort to more precisely characterize the reference detector pickoff. Substantial fluctuations in source pulse energies prevented the empirical derivation of transmission and reflection coefficients; therefore, a transmission to reflection ratio was generated. This only required the two existing detectors; one measuring transmitted power and the other simultaneously measuring reflected power. No focusing lenses were used given the source's instability at lower pump current levels and the detectors' low saturation levels.
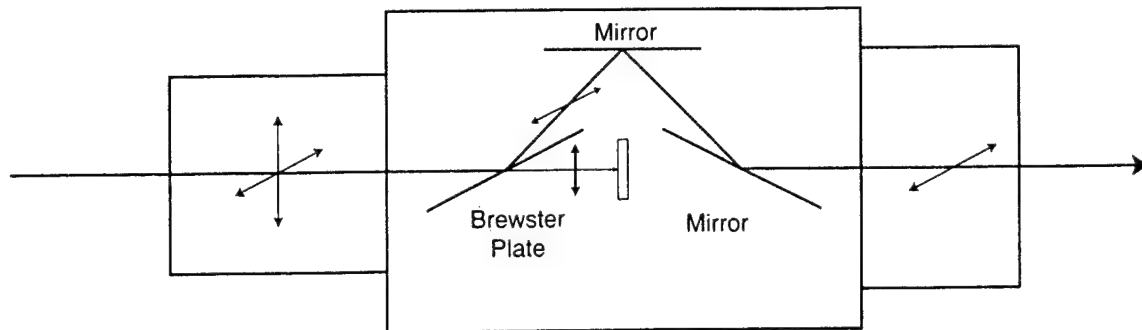
Figure 7 – Cleveland Crystals Model 1600 IR Polarizer

This reference signal is then attenuated using a fixed and characterized neutral density filter to prevent saturation of the reference detector. A focusing lens is used to ensure that the reference detector collects all of the power transmitted through the filter. The output of the detector is amplified using a transimpedance amplifier and then routed to channel one of an oscilloscope.

The beam transmitted through the second CaF_2 pickoff is then transmitted through a CaF_2 50/50 beamsplitter oriented at 45° and onto the target sample (see Section 4.2.4). A portion of the reflected energy from the target is then reflected by the beamsplitter into the target detector leg of the system. The target signal is then routed through a wideband polarizer in order to observe the effects of depolarization caused by the target sample (refer to Section 4.2.6). The polarizer uses a Brewster plate to pass the in-plane, or p, polarization and reject the out-of-plane, or s, polarization. The p-polarization is then internally dumped and the s-polarization is reflected onto two simple turning mirrors to produce an s-polarized output as shown in Figure 7. Manufacturer's specifications state a throughput near 50% at the required wavelengths and a 2000:1 nominal polarization ratio

[6]. The polarizer is simply rotated 90° about the propagation axis to output system p-polarized[2] light.

The polarizer is also necessary in the monostatic system to determine the necessary reflection coefficient of the 50/50 beamsplitter for the reflected energy, since reflective properties vary significantly between s and p-polarizations. The output of the target detector is also amplified using a transimpedance amplifier and then routed to channel two of an oscilloscope.

3.3 Data Acquisition and Control Electronics and Detectors

Careful consideration was placed on selecting a detector and amplifier combination capable of detecting throughout the desired 1.5µm - 5.0µm band. The EG&G (now PerkinElmer) Optoelectronics J10D indium antimonide (InSb) infrared photodiode detector was chosen due to its 1.0µm - 5.5µm wavelength range. The 77°K operating temperature allowed for integration of a 20° cold field of view (FOV). The cold FOV was necessary to improve detectivity and reduce unwanted background current I_{BG} [18]. Also, one property of InSb photovoltaic detectors that is not fully understood is the change in detector quantum efficiency with changes in operating temperature [8]. This change in quantum efficiency further affects detectivity, which rolls off at 110°K for the J10D series.

This detector has a manufacturer's estimated responsivity of 3 A/W and can operate at the 10 kHz repetition rate defined by the source. A J10D-M204-R250U and J10D-M204-R500U with 250µm and 500µm diameter respective apertures were available

---

[2] The polarizer outputs s-polarized light, with respect to the Brewster plate, regardless of orientation.

for use. Detector specific specifications were necessary to determine which would be best

suited in the roles of reference and target detector.

Table 1 - PerkinElmer Optoelectronics InSb Detector Specifications

Model Number	J10D-M204-R250U[3]	J10D-M204-R500U
Active Diameter (mm)	0.25	0.50
Peak Responsivity (A/W)	3.0	3.9
Peak D* (cmHz$^{1/2}$/W)	1.0 x 10^{11}	5.6 x 10^{11}
NEP (W/Hz$^{1/2}$)	2.0 x 10^{-13}	8.7 x 10^{-14}
Saturation (mW/cm^2)	200	200
Band (μm)	1.0 – 5.5	1.0 – 5.5

Table 1 contains the necessary quantities to calculate the operating range for each

of the detectors. A desired minimum signal-to-noise (SNR) ratio of 10 was chosen setting

the minimum acceptable power level at 2.0 x 10^{-12} W for the R250U detector and

8.7 x 10^{-13} W for the R500U. Saturation thresholds of 98.2 μW and 393 μW were

calculated respectively. These values were used to determine the appropriate neutral

density filter necessary to keep the reference detector within its operating range.

Assuming that all of the power incident upon the reference detector focusing lens is

focused onto and does not exceed the active area of the reference detector, either the

R250U or R500U may be used.

The selection process for the target detector involved the operating range of the

detector and the type of targets (diffuse or specular). A larger active area and lower noise

equivalent power (NEP) are desirable, especially when dealing with poorly reflecting

diffuse samples; therefore, manufacturer estimates for NEP and active diameter were

compared. Since the majority of the target samples to be characterized were expected to

---

[3] Specifications for the J10D-M204-R250U are estimates provided by the manufacturer.

be diffuse and due to its 300% larger active area, the R500U was selected as the target detector. The actual NEP for the R500U was ignored due to the lack of actual specifications for the R250U. Caution is necessary in this configuration, when aligning the system or characterizing an unknown sample, to prevent over saturation and damage to the target detector.

The PerkinElmer PA-7 current mode transimpedance amplifier was selected due to its low current noise and selectable high gain of 10^7 V/A. The output of the transimpedance amplifier is fed into the oscilloscope where voltage is measured. The combination of detector and preamplifier results in an overall estimated system voltage responsivity of 3 x 10^7 V/W, which is used to determine reference and target detector power. Given the lack of actual specifications on the J10D-M204-R250U, simultaneous measurements were taken using a known Lambertian reflectance standard in order to calculate a relative current responsivity ratio, which is expected to vary spectrally. Figure 8 graphically depicts the method used for detector calibration. A 4:1 voltage and power ratio is expected, when each detector is separately connected to the same transimpedance amplifier and assuming the fluctuation in incident radiation levels to be negligible, as a result of the 4:1 ratio in active areas. A 3.95:1 voltage ratio was observed and combined with a 3.42:1 voltage ratio when connected to their respective pre-amplifiers to produce a 1.16:1 current responsivity ratio[4]. Since the BRDF is a ratio of incident and reflected powers, actual responsivities are unnecessary and allow the calculated ratio to be used in post-processing to calibrate the collected data.

---

[4] The ratios presented are valid only at 1.046μm.
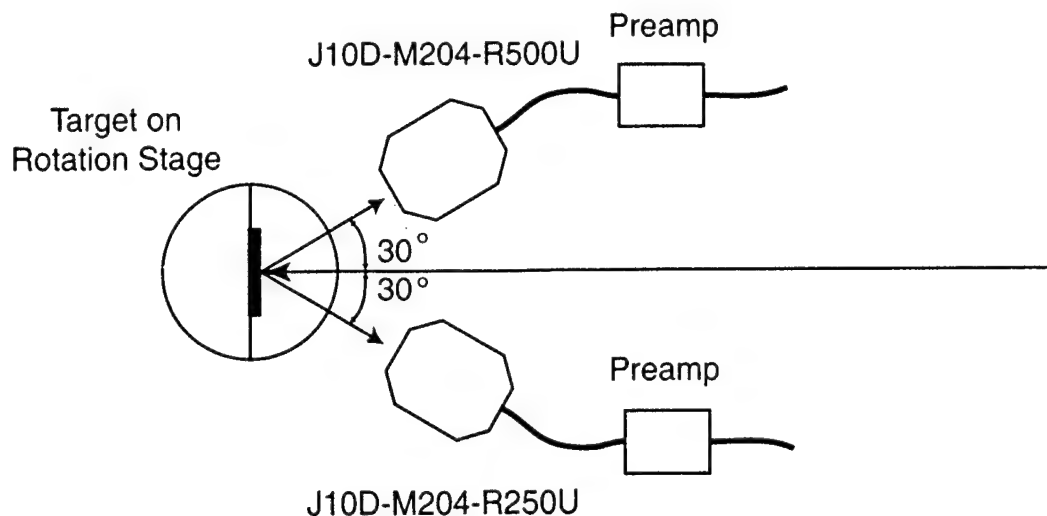
Figure 8 – Laboratory Setup for InSb Detector Calibration

The power measured at each of the detectors is then back propagated through the optical components to determine the power incident upon and reflected by the target sample. These powers along with the solid angle subtended from the target to the target detector and the target angle are used in the BRDF calculation, Equation (2).

The Lecroy 9450A dual channel 300 MHz oscilloscope was chosen to display and process the data collected by the detector/preamplifier system. The q-switched pulse from the source is used as an external trigger freeing channels one and two for reference and target signal data respectively. Internal processing is performed in order to reduce the effects of time variations caused by the source, detectors, amplifiers, optics, or speckle. The time base is selected such that a single pulse is visible and then a summed average of 1000 sweeps is taken for each channel at each wavelength and target position. This data is stored in oscilloscope memory until the time base is cycled instructing the scope to start the process over. The oscilloscope is queried between cycles by the data acquisition and

control computer to retrieve the averaged data, which is later transferred for post-processing.

The data acquisition and control computer is also used to control the Newport 855C programmable controller, which in turn controls the Newport 495-A single-axis rotation stage. A three-axis adjustable mount is placed onto the rotation stage to ensure that the incident beam is normal to the target surface when the stage is set to $0°$. Adjustments were made using a highly specular target to maximize the target detector return and allow for visual alignment. A single-axis translation stage is also placed beneath the 495-A to center the rotation axis of the stage on the incident beam. This step is crucial in order to prevent the solid angle, which is a function of the target to detector distance, from changing with the rotation angle. A walk-off in the measured reflected energy and BRDF for a Lambertian target sample is a good indicator of a misalignment, since intensity (in this case – P_r/Ω_r) is a function of the (varying) solid angle.

3.4 Data Collection Procedure

In order to characterize the target samples provided by AFRL/SNJM, the measurement system itself had to be calibrated. Essentially, all optical components downstream from and including the reference detector branch would need to be characterized for both s and p-polarizations. The horizontal linear polarization in this experiment is considered, system wide, to be p-polarized since the plane-of-incidence on the CaF_2 optics and the target stage is horizontal. Focus is shifted to the target stage after obtaining the transmission to reflection ratio for the reference detector pickoff, the attenuation coefficient for the reference detector neutral density filter, the transmission and

23

reflection coefficients for the 50/50 beamsplitter, and the transmission coefficient for the wideband polarizer for both polarizations.

As mentioned previously, the target must be centered, in the horizontal plane, on the vertical rotation axis of the rotation stage to prevent any angular bias. This is accomplished by placing a plumb bob over the target, which is centered on the rotation axis of the stage. Adjustments are made to the target so that the bob is allowed to make contact with the target but not allowed to move as the sample is rotated from -46° to +46°. Next, the incident light is centered on the target sample by translating the rotation stage perpendicular to the propagation axis.

To ensure that the reflected energy path is equally aligned, a highly specular target is placed onto the stage. An iris is then placed between the target and beamsplitter and the stage is placed at 0°. Alignments are then made to the tip, tilt, and translate capable target sample mount to send the reflected signal back through the aperture of the iris. Next, the wideband polarizer is oriented such that the beam reflected by the 50/50 beamsplitter is centered on the input and output apertures of the polarizer. This is a crucial step in the alignment process given that it ensures that the reflected signal is incident upon the polarizer Brewster window at Brewster's angle.

To prevent over saturation and possible damage to the target detector, a partially transmissive cover is placed over the input aperture. The detector is then aligned to maximize the peak voltage output displayed on channel two of the oscilloscope. Alignments of the reference detector are also made to maximize channel one peak voltage. Figure 9 displays both reference and target detector pulses at a 0° target angle of incidence and reflection and at 1.046µm.
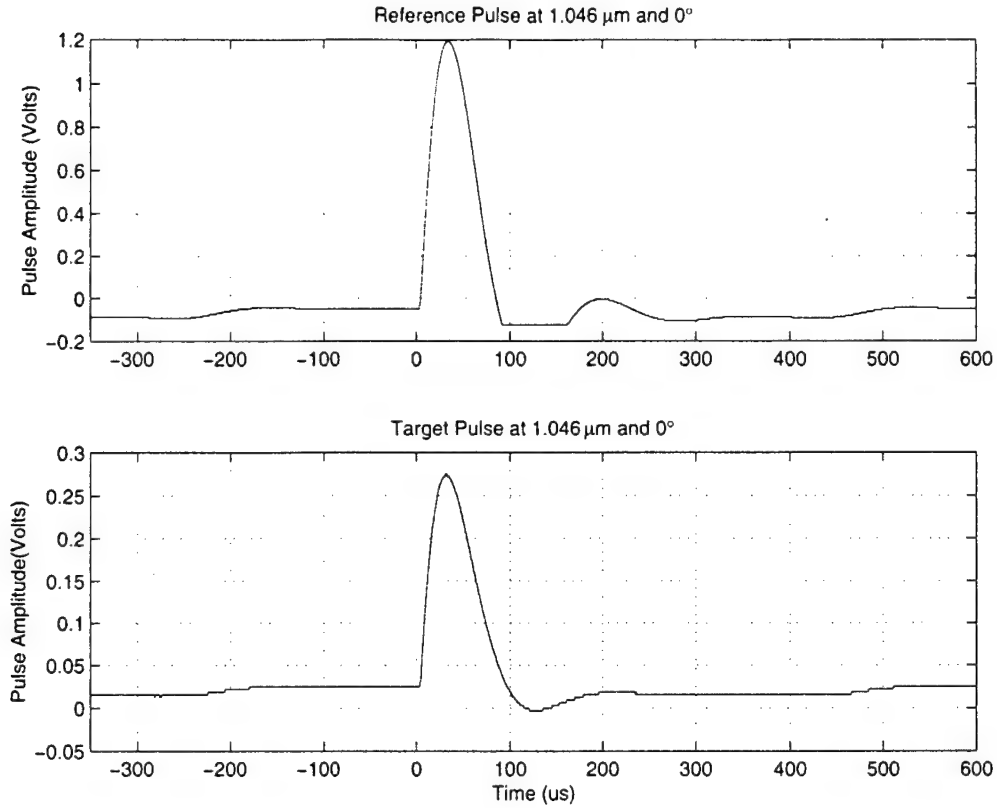
Figure 9 – Summation Averaged Voltages Pulses for Reference and Target Detectors

Following the empirical determination of the optical component properties and system alignment, a known Lambertian calibration standard is placed onto the target stage. A Lambertian surface adheres to Lambert's cosine law, which states that the reflected or transmitted luminous intensity in any direction from an element of a perfectly diffusing surface varies as the cosine of the angle between that direction and the normal vector of the surface. As a consequence, the luminance of that surface is the same regardless of the viewing angle [17].

Equation (4) defines the radiant flux collected by the detector, allowing the angle formed between the surface normal line of the source and the line between the source and detector to be nonzero. It also accounts for the case where the detector surface normal does not coincide with the line between the source and detector. Refer to Figure 10 for a graphical representation of Equation (4).

$$\phi_d = L_s A_s \Omega_d$$

$$= L_s A_s \cos\theta_s \frac{A_d \cos\theta_d}{\left(r\!\!\Big/ \cos\theta_s \right)^2} \tag{4}$$

The system configurations outlined in Section 4.1 fix θ_d at approximately zero since no (useful) additional information can be obtained by varying this angle; this also reduces target characterization time significantly. However, the source (or target in this case) is rotated causing variations in θ_s. These variations influence the BRDF measurement due to the definition of radiance in terms of flux per unit projected area per unit solid angle. The projected area, $A_{s\perp}$, is the surface area of the source (or the illuminated portion of the target), A_s, as seen from the detector.

$$A_{s\perp} = A_s \cos\theta_s \tag{5}$$

A planar 100% Lambertian source will theoretically produce a $1/\pi$ BRDF, which is constant over the rotation range. Since reflected radiance is constant throughout the entire
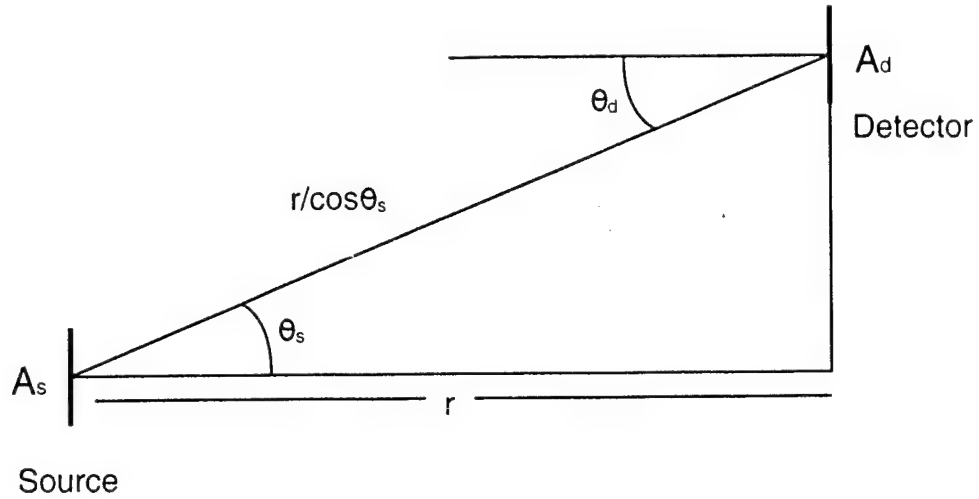
Figure 10 – Cosine-to-the-Fourth ($\cos^4$) Law [8]

hemisphere for Lambertian targets, the following relationship

$$M = \pi L \tag{6}$$

holds, where M is the exitance and L is the radiance from the source (or target). The proportionality is π instead of 2π because of the integration of the projected area factor for various portions of the hemisphere into which the source radiates. This proportionality factor is derived from the following relationship

$$
\begin{aligned}
M &= \frac{\partial \varphi}{\partial A_s} = \int_{\Omega_d} L \cos \theta_s \, \partial \Omega_d \\
&= \int_0^{2\pi} \partial \varphi \int_0^{\pi/2} L \cos \theta_s \sin \theta \, d\theta \\
&= 2\pi L \frac{1}{2} = \pi\, L
\end{aligned}
\tag{7}
$$

where the Lambertian-source assumption has been used to pull L outside of the angular

integrals [8]. Therefore, in the case of the 99% Lambertian reflector used in this

experiment, the BRDF as a function of source (or target) angle should remain constant at

$0.99/\pi$.

The 99% Lambertian reflector mentioned is used for system calibration in this

experiment. Prior to taking measurements, the detector and target are oriented such that θ_s

(or θ_r) and θ_d are zero. The target sample and θ_r are then rotated from -46° to +46°, with

respect to the light propagation axis, in 2° increments at each wavelength. At each rotation

angle, 1000 single pulse sweeps are collected and summation averaged for both the

reference and target detectors to reduce the effects of time variations. The pulse must also

be smoothed prior to post-processing in order to reduce the effects of oscilloscope

bandwidth limitations. The ASCII data is stored in separate files for each detector at each

rotation angle and wavelength. A graphical depiction of this data is shown in Figure 9.

Post-processing begins after collection of the Lambertian sample data for a given

wavelength (refer to Appendix A for a sample of the Matlab code used to calculate the

BRDF). Peak voltage is calculated for each detector pulse by averaging the baseline noise

level data prior to the rise of the pulse and subtracting it from the peak voltage measured;

data after the pulse is neglected due to overshoot and oscillations. Once the peak voltage

is determined, a conversion to peak power is calculated using the calculated voltage

responsivity at the given wavelength. This data is then fed into the BRDF calculation

along with the fixed solid angle, Ω_r, and the variable target angle, θ_r. A loop accomplishes

these calculations for each target angle and produces a BRDF vs. target angle plot. The

resultant BRDF should be constant with respect to the target angle at $0.99/\pi$.
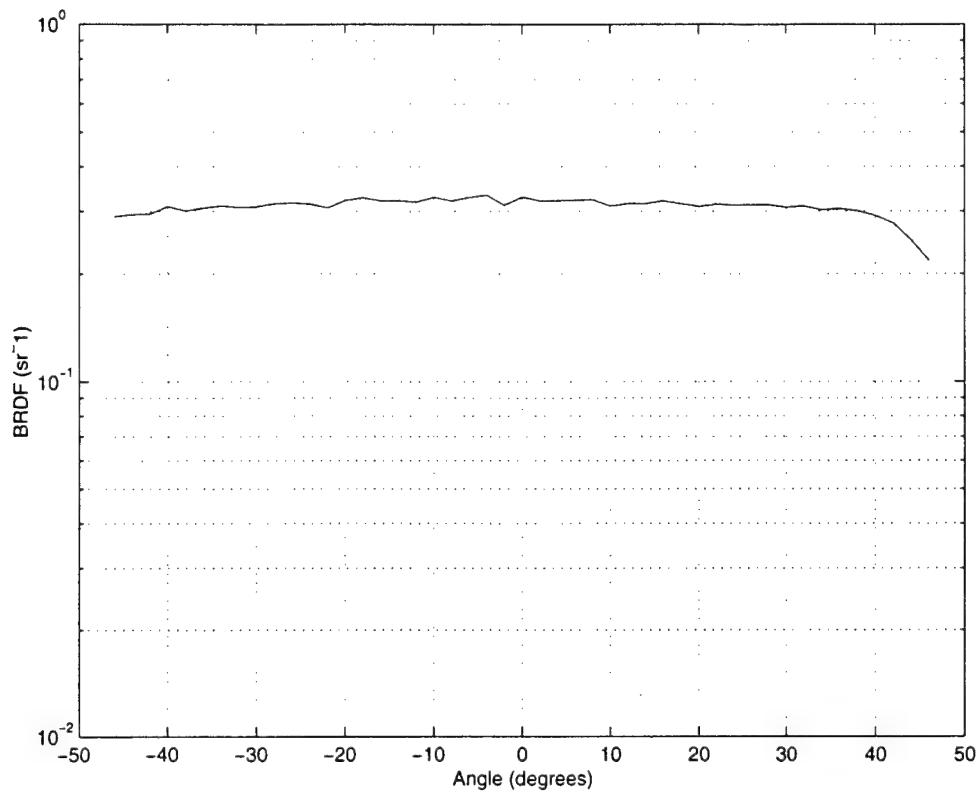
Figure 11 – Sample BRDF for 99% Lambertian Calibration Standard

Figure 11 displays the results of a 99% Lambertian target at 1.046μm after the system calibration factor was applied. This system calibration was applied to all target sample post-processing algorithms in order to reduce the effects of any uncertainties in optical component characterization.

IV. Data and Error Analysis

This chapter presents the results obtained using the monostatic BRDF measurement system shown in Figure 5 and introduces a bistatic version and its results. The data presented incorporates a known Lambertian reflectance standard (Labsphere SRS-99-020) to produce a system calibration factor, which is applied to the collected data.

All collected data was limited to the Nd:YLF output of 1.046μm due to numerous difficulties with the Q-Peak LADAR frequency doubling crystal, Ti:S cavity alignment, and RTA OPO. The incident light was also restricted mainly to horizontal or p-polarization in the monostatic configuration due to problems with the CaF_2 50/50 beamsplitter.

4.1 System Configurations and Associated Results

4.1.1 Results Using the Monostatic Measurement System Shown in Figure 5 (Case 1)

The data presented in this section was collected using the monostatic approach shown in Figure 5. The mean of the BRDF was adjusted by multiplying a correction factor against the BRDF calculation to produce a mean of $0.99/\pi$. Figure 12 shows the BRDF data collected for this particular system configuration. A standard deviation of 0.045 was found resulting in a 14.29% error (calculated by dividing the standard deviation by the mean). Figure 13 shows the relationship between the reference and target detector powers along with the cosine of the target rotation angle[5].

---

[5] The relationships are slightly exaggerated due to a multiplicative shift in the reference and target data.
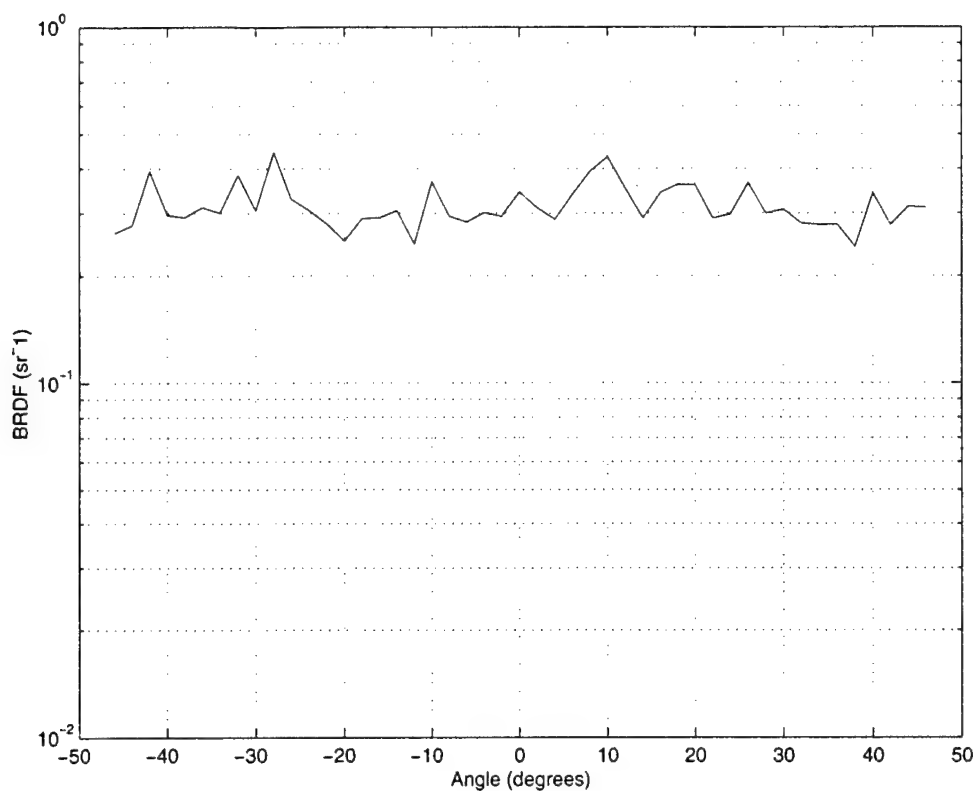
Figure 12 – Monostatic BRDF for 99% Lambertian Calibration Standard

The collected target power is expected to fall off with the cosine of this angle due to the radiometric properties of the Lambertian sample as previously described. The target data does appear to track the cosine; however, the deviation from this line is more obvious and clearly responsible for the large calculated BRDF error.

Statistics were also performed on the reference power to determine the perceived stability of the source. A reference drift of 5.15% was observed for this data set, which may have affected the BRDF calculation, if only a portion of the reference branch power is incident upon the active area. Incident beam uniformity (or symmetry) is required to reduce the BRDF calculation from differential to absolute form; this is also true for the reference beam when only a portion of the signal is collected. Unfortunately, a focusing

31
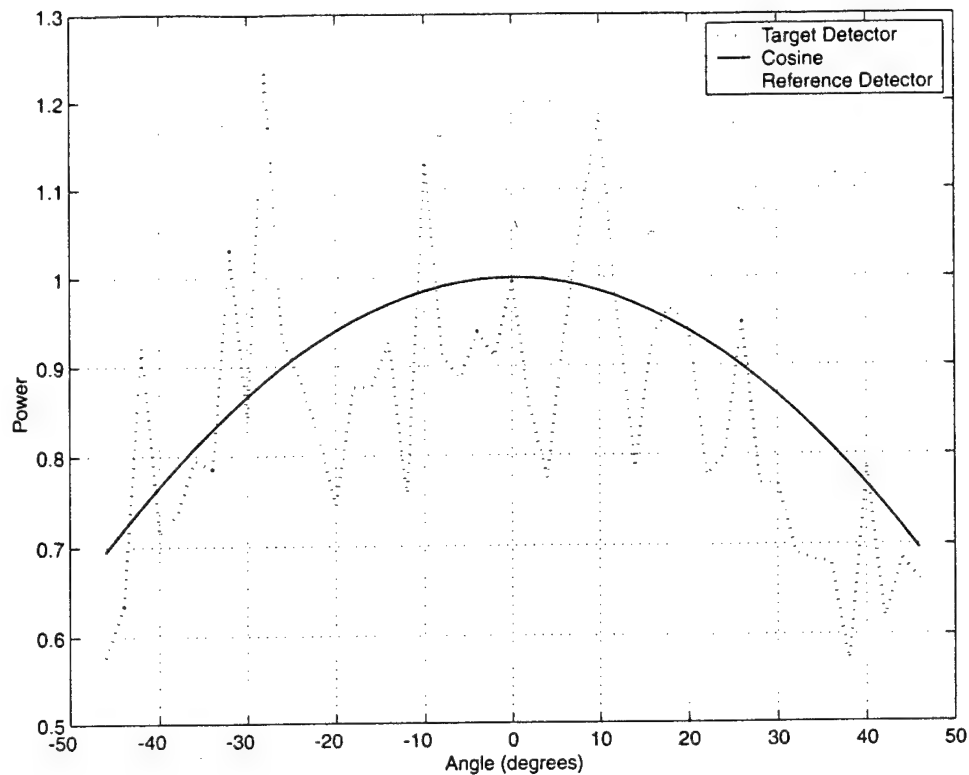
Figure 13 – Shifted Reference and Target Power for 99% Lambertian Calibration Standard[6]

lens does not guarantee that all of the power in the reference branch is collected by the reference detector, nor does it remove the effects of source spatial variation in this branch.

Another potential source for error in the monostatic configuration is the beamsplitter. As mentioned previously, a highly specular target is used during the target detector alignment process. This particular target reflects sufficient power to visibly detect the energy reflected by the beamsplitter, with the assistance of an infrared detection card. When this card is placed in the target branch of the system, two spots are observed originating from the front and rear surfaces of the beamsplitter (refer to Section 4.2.4 for further discussion on this topic).

---

[6] Detector powers were shifted to fit on a single plot with the cosine of the target angle.

4.1.2 Results Using a Modified Monostatic Measurement System (Case 2)

In an effort to remove the reference detector as a substantial error source, the J10D-M204-R500U (500μm) detector was relocated to the reference branch and the J10D-M204-R250U (250μm) detector assumed the role of target detector. In this configuration, the wideband polarizer is removed due to insufficient power at the target detector. This drastically increases the uncertainties associated with beamsplitter reflectivity, since diffuse reflectors tend to depolarize incident radiation and the reflectivity of the beamsplitter is a strong function of polarization (especially near Brewster's angle). Therefore, the results are meant to be purely qualitative.

An increase in source pump current is removed as a potential remedy due to source instability at higher pump levels and concern regarding reference detector over saturation. However, depolarization of the reflected energy for the Lambertian sample was empirically determined to be minimal, allowing the polarizer to be removed from the system and replaced in the post-processing code with a transmission coefficient of 1.0 (as a rough approximation).

While the BRDF in Figure 14 does appear to track the desired $0.99/\pi$ mean, the standard deviation has increased more than twofold resulting in an error of 36.2%. This increase in error is believed to be a direct consequence of speckle effect, described in Section 2.3, and a substantial reduction in reference detector power through 0° into the positive angles. Measurement of target reflected power in the reference branch is believed
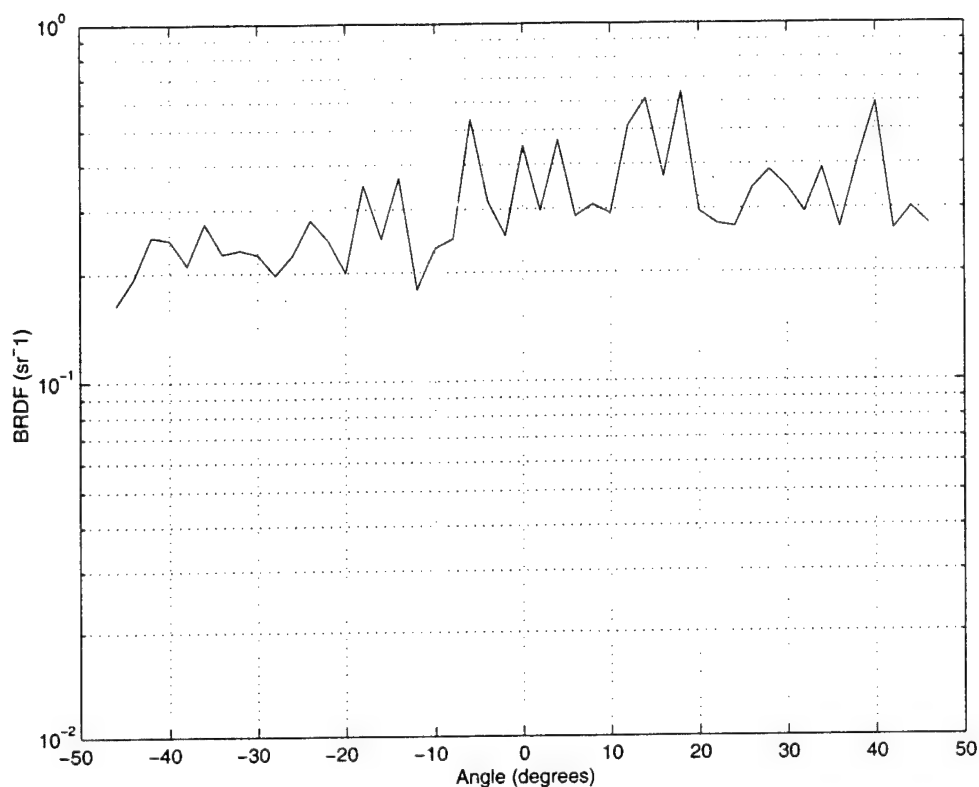
Figure 14 - Monostatic BRDF for 99% Lambertian Calibration Standard Using J10D-M204-R250U as the Target Detector

to be responsible for the increased reference drift observed in these cases (shown in Figure 13). This may be attributed to energy reflected directly from the target into the reference detector, since both detectors are located on the negative target angle side of the incident beam propagation axis.

Target incident power was also increased in response to a 75% loss in target detector active area; therefore, the effects of reflected power in the reference branch were amplified. A steady increase in BRDF into the positive angles is also noted and is believed to be the result of target misalignment. Measures were then taken to reduce this error by placing more effective beam dumps around the reference detector.

The 75% decrease in active area results in a 75% decrease in the average number of collected speckle. In fact, the average number of speckle collected by the J10D-M204-R250U is less than four at a wavelength of 1.046μm, a target distance of 79.4 cm, and a spot size of 6.4 mm. However, the amount of speckle collected may have been increased to that of the J10D-M204-R500U if the target distance were simply decreased by 50%. Again, the resultant data in this configuration is purely quantitative and was used to illustrate the benefits associated with larger active areas. It should again be noted that the energy in the reference branch is focused onto the reference detector, thus considerably decreasing the effects of spatial variation in the source and reducing (not removing) the need for larger active areas.

4.1.3 Results Using a Modified Monostatic Measurement System (Case 3)

Since similar fluctuations in reference branch power were observed for both detectors in Case 2, the R500U was returned to the target detector location and the R250U reassumed the role of reference detector. Up to this point, focusing lenses had not been used to focus the reflected energy onto the target detector due to uncertainties regarding the calculation of the solid angle. This uncertainty centers on the placement of the focusing lens. If the radiation incident upon the target is collimated and the target is perfectly specular, the reflected energy should also be collimated and require the lens to be placed exactly one focal length from the detector. In the case of a diffuse or Lambertian target, the reflected radiation can no longer be assumed collimated. Instead, the reflected energy is diverging at an angle subtended from the target to the aperture stop defined by the rim of the lens (or polarizer input aperture in this case). In this situation, the lens must

be placed greater than one focal length from the detector in order to focus the energy into the same area. Decreasing the solid angle by increasing the distance between the target and the target detector would reduce this error but at a substantial cost.

One efficient method of reducing this error is to increase the separation while maintaining the solid angle through the use of a larger diameter lens. Unfortunately, little is accomplished since the aperture stop is not defined by the lens rim in this measurement system. With the wideband polarizer removed, such as in Case 2, the maximum useful diameter of the lens is further restricted by the FOV of the detector (a 20° cold FOV in this case). Another option, which does not require an increase in separation, is to maximize the active area of the detector without sacrificing performance. While the latter option is more costly, it may be necessary to ensure that all, or at least a known portion, of the reflected energy is sampled by the detector. Careful consideration must also be given to the selection of the focusing optic substrate given that some materials are more susceptible to chromatic aberration. Since the thin-lens equation

$$\frac{1}{f} = (n_l - 1)\left(\frac{1}{R_1} - \frac{1}{R_2}\right) \tag{8}$$

is wavelength-dependent via $n_l(\lambda)$, the focal length must also vary with λ [14]. This type of aberration induces a lateral shift in focal lengths for varying wavelengths, which may cause the focused energy to overfill the active area of the detector.

In a qualitative effort simply to determine if a reduction in speckle size will reduce the observed BRDF error, a focusing lens is placed in front of the wideband polarizer input aperture. Placing the lens before the polarizer increases the solid angle and the amount of

36
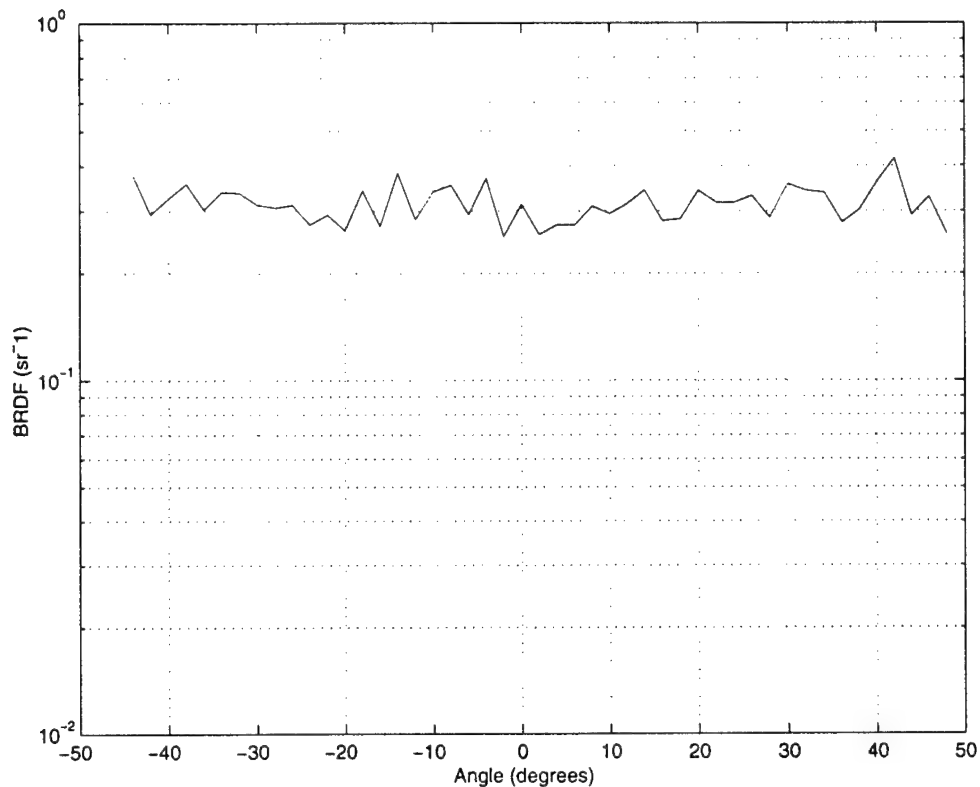
Figure 15 - Monostatic BRDF for 99% Lambertian Calibration Standard While Focusing Reflected Power onto the J10D-M204-R500U Target Detector

speckle collected, provided the focal length of the lens is longer than the polarizer. Typically the focusing lens rim will define the active area in the solid angle calculation; however, the angle subtended from the target to the polarizer input aperture rim was sufficiently smaller than the angle defined by the lens in this case.

Figure 15 displays the results of focusing the reflected power onto the target detector. The BRDF error was reduced to 11.6% corresponding to a 19% decrease in error when compared to case 1, shown in Figure 12. At this point, static data was collected to ensure that the oscilloscope processing algorithm and the post processing code were not contributing to the observed errors. A BRDF error of 1.1% was calculated, decreasing the

likelihood that data processing was responsible for a significant portion of the error. Another interesting aspect to this discovery is that speckle does not appear to be as prevalent in the static case. Since speckle is both time and spatially variant, one might expect to see errors on the order of those observed in its corresponding dynamic case. However, these results suggest that the spatial variation exceeds any time variation in the speckle, which further suggests that the sample surface and possibly Rayleigh, defect, or topographic scatter may be responsible for what appear to be fringes. Another indication that spatial variance exceeds time variance is the fact that the reference detector power fluctuation no longer exceeds 3%[7].

4.1.4 Results Using a Bistatic Measurement System (Case 4)

At this point, a paradigm shift was necessary to reduce the errors without sacrificing the integrity of the collected data. In the monostatic arrangement, the input aperture to the polarizer defines the solid angle and the polarizer is essential in the characterization of the energy reflected by the beamsplitter. Also, too many uncertainties surround the use of a focusing lens on the target detector. These two limitations led to the development of the bistatic configuration shown in Figure 16. The measured BRDF is displayed in Figure 17.

---

[7] This statistic follows steps taken to ensure that reflected target power is not collected by the reference detector.
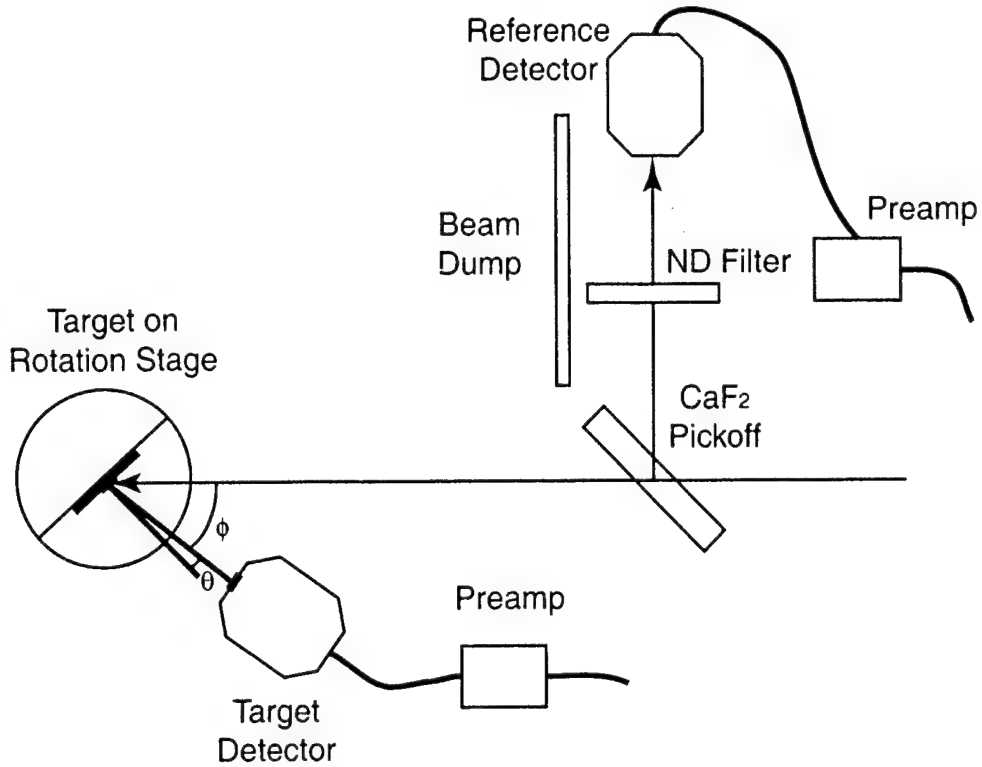
Figure 16 – Bistatic BRDF Measurement System

For the bistatic case, the following relationship is used to define the intensity

observed by the detector

$$I = L l_c A a_c = L\cos(\theta_r + \phi) A\left(\frac{\cos(\theta_r)}{\cos(\theta_r + \phi)}\right)$$

$$= LA\cos(\theta_r) \tag{9}$$

where L is the radiance at the target and A is the actual area of the target illuminated by the

incident light. Two correction terms are applied to calculate the intensity as seen by the

offset, but in-plane, detector. The correction factor, l_c, adjusts for the variation in radiance

associated with changes in the actual area illuminated. The correction factor, a_c, adjusts
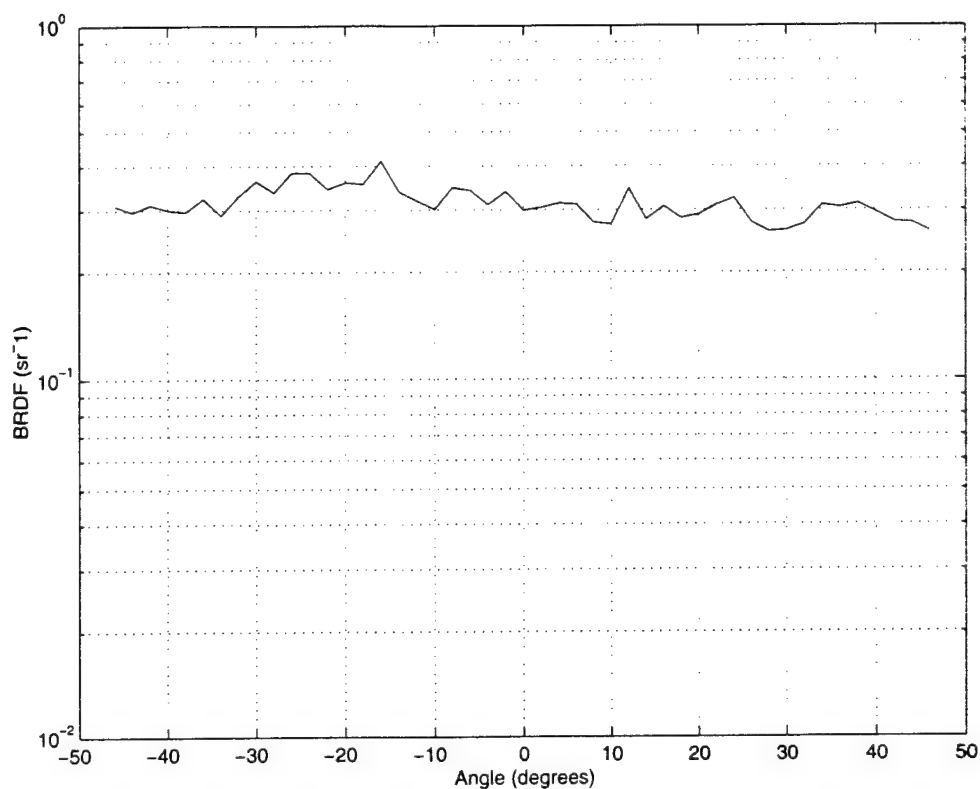
Figure 17 - Bistatic BRDF for 99% Lambertian Calibration Standard

for the illuminated area as viewed from the detector while ϕ defines the angle between the incident light propagation axis and the detector active surface normal. The point where the target surface and detector active surface normals overlap defines the new position at which $\theta_r = 0°$. This results in a final correction factor, $\cos(\theta_r)$, that matches the monostatic case.

In this configuration, the beamsplitter is removed which removes the uncertainties associated with front and rear surface reflections. The wideband polarizer is also removed since it is no longer needed to characterize the beamsplitter[8]. This also allows the target

---

[8] The polarizer is also necessary to observe the depolarization effects of the target; however, a higher SNR was more desirable in this case.

detector to be placed closer to the target which, in turn, increases the amount of speckle collected by the detector. However, this also increases the solid angle and may adversely affect the calculation of the BRDF in absolute form. Recall that the reflected differential intensity is reduced to absolute form only when the power on the active surface of the target detector is assumed uniform. Therefore, the detector aperture size must be limited with respect to the reflected intensity fluctuations (as a function of θ_r) and is thus a function of the target's reflective properties (specular, diffuse, or both). In other words, the target detector's aperture may be increased with increasingly diffuse targets.

The new configuration produced a 10.9% BRDF error. A slight shift in the data, due to uncertainties regarding the true reflected angle, reduced the error to 9.3%. This data is most easily compared with that of Case 1, since no focusing lenses are used and the J10D-M204-R500U is in the target detector position. The BRDF error in Case 1 is expected to exceed that of Case 4, given that the solid angle is reduced, causing a reduction in collected speckle. In fact, a 23.7% reduction in BRDF error is observed. However, the results may have been influenced by a wet sand resurface of the calibration standard prior to data collection. This effort was primarily aimed at reducing topographic and defect scattering and was recommended by Labsphere[9].

4.1.5 Results Using Bistatic Measurement System and Biased Silicon Photodetectors (Case 5)

All cases prior to Case 5 have utilized the J10D series InSb detectors defined in Section 3.3. In an effort to reduce the effects of speckle, these detectors were removed

---

[9] 220-grit waterproof sand paper was used due to nonavailability of the recommended emery cloth.

from the system in favor of the Electro-Optics Technology ET-2010 biased silicon

photodetector. Table 2 lists the manufacturer's specifications for this detector.

Table 2 - Electro-Optics Technology ET-2010 Silicon Detector Specifications

Model Number	ET-2010
Active Diameter (mm)	.564
Peak Responsivity (A/W)	0.4
NEP (W/Hz$^{1/2}$)	<1.0 x 10^{-13}
Saturation (mW/cm^2)	10
Band (nm)	300 - 1150

These detectors obviously do not satisfy the required 1.0µm - 5.0µm measurement

range; however, they provide an acceptable 0.11 A/W (28% of peak) responsivity at the

(limited) 1.046µm wavelength. The 27.3% increase in active area is of particular interest

in this case. These detectors were simply integrated into the bistatic system configuration

described in Case 4, maintaining the target to detector distance and newly defined rotation

point for $\theta_r = 0°$. This also increases the solid angle by 27.3%, but is not expected to force

the BRDF equation into differential form since the targets of interest are more diffuse than

specular. Figure 18 shows the corresponding BRDF vs. θ_r results.

The bistatic configuration allowed for the collection of the sample's response to

vertically polarized incident light. These results are also included in Figure 18 and closely

match those of the horizontal component as expected. BRDF errors of 6.4% and 5.5%

were observed for horizontal and vertical polarizations respectively, which corresponds to

a 15.6% improvement (for horizontal) over the results obtained in Case 4. The drop off at

+40° is believed to be a calibration source error at large angles. The target surface normal

varies from -46° to +46° with respect to the incident light source propagation axis in the
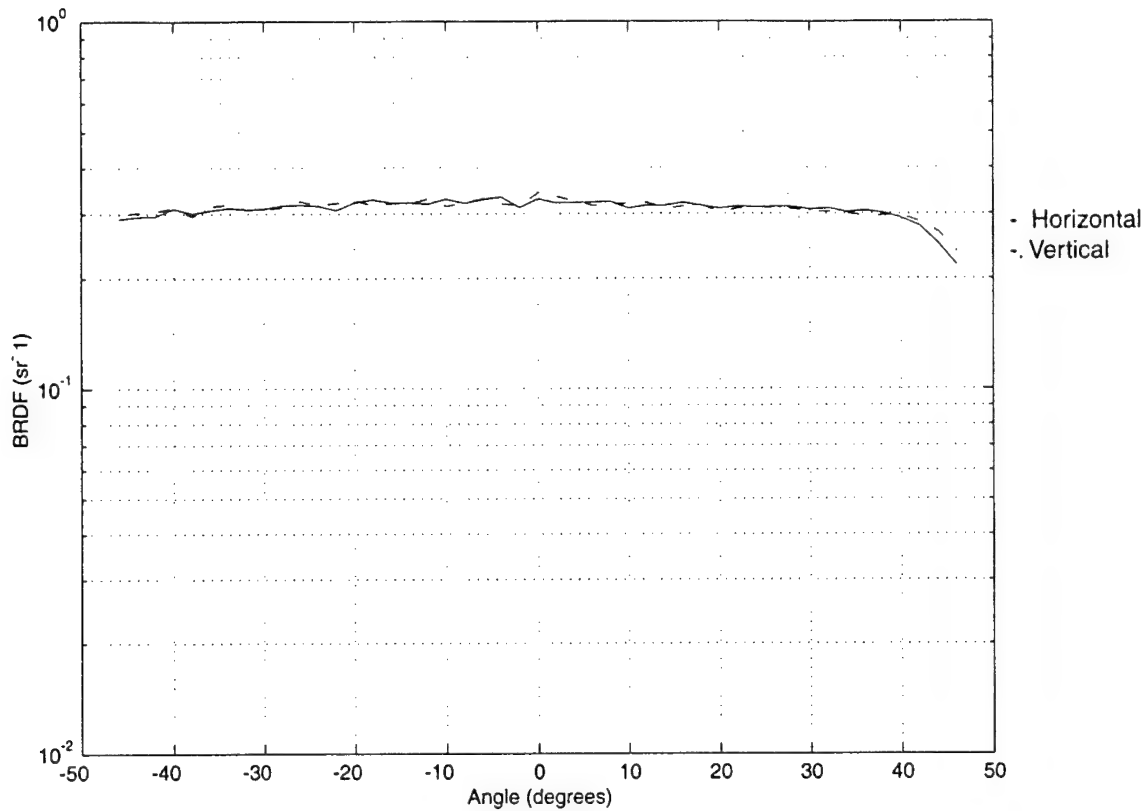
Figure 18 – Bistatic BRDF for 99% Lambertian Calibration Standard Using Silicon
Photodiodes

monostatic case. However, in the bistatic case, these angles range from -16° to +76° due

to a 30° target detector offset. Also, Labsphere verification tests fix the incident flux at 8°

from normal and measure the reflected energy using an integrating sphere [24]. This does

not adequately characterize the sample for the purpose of this experiment; therefore, θ_r is

limited to +/-40° so as to more accurately establish the BRDF measurement system error.

By limiting θ_r to +/-40°, system errors of 2.8% and 3.3% are obtained for the

horizontal and vertical polarizations respectively. This corresponds to a 75% improvement

(for horizontal) over Case 4.
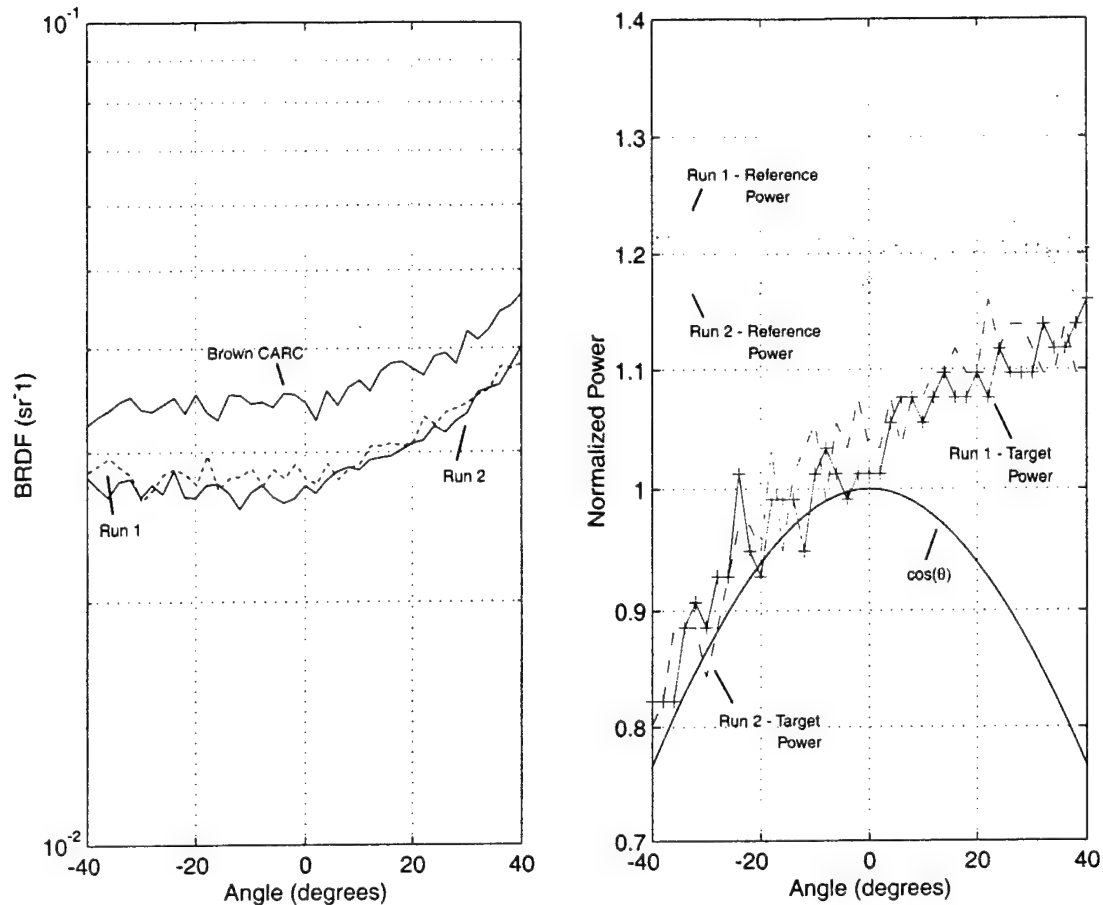
Figure 19 - Bistatic BRDF for 10% Lambertian Calibration Standard and Brown CARC Paint Using Silicon Photodiodes

4.1.5.1 Verification of the Bistatic Measurement System and Biased Silicon Photodetectors Using 10% Lambertian Reflector

The Labsphere Spectralon SRS-10-020 10% Lambertian calibration standard was used to verify the validity of the system calibration factor applied to the post-processing code resulting from the measurements in Case 5. The expected BRDF value for such a sample is 10% of π^{-1} or 3.183×10^{-2}, but this was never achieved. Figure 19 shows the results of two p-polarized data runs that suggest that the incident beam was right of the target's rotation axis. The runs produced 11.9% and 10.6% errors respectively. Run 2 is

the result of realignment and target resurfacing, which reduces the probability that misalignment or topographic scatter is responsible. A brown green chemical agent resistant coating (CARC) paint sample exhibited markedly similar results and its BRDF is also provided in Figure 19.

4.1.5.2 Results Using Bistatic Measurement System and Biased Silicon Photodetectors to Characterize Green CARC Paint

Despite the unsatisfactory results obtained for the 10% Lambertian standard and Brown CARC paint, a sample of Green CARC paint was characterized using the 99% Lambertian system calibration factor. This particular sample was chosen so that results could be compared with the existing data from another BRDF measurement system and due to its expectedly higher reflectance properties [19]. Unfortunately, the prior results are limited to the $1.58\mu m - 1.8\mu m$ band making the comparison purely qualitative. Figure 20 shows the data collected by the post-calibrated bistatic system described in Case 5 and the results collected by a previous monostatic system.

This sample is clearly diffuse and appears to be even more Lambertian than the Labsphere standard. A 2.4% deviation was observed at $1.046\mu m$ without data manipulation compared to the 2.7% error found in Case 5 after limiting the target's angular range. A qualitative comparison of both sets of results shows a trend toward increased reflectivities at higher frequencies, which lends additional credibility to the results obtained.
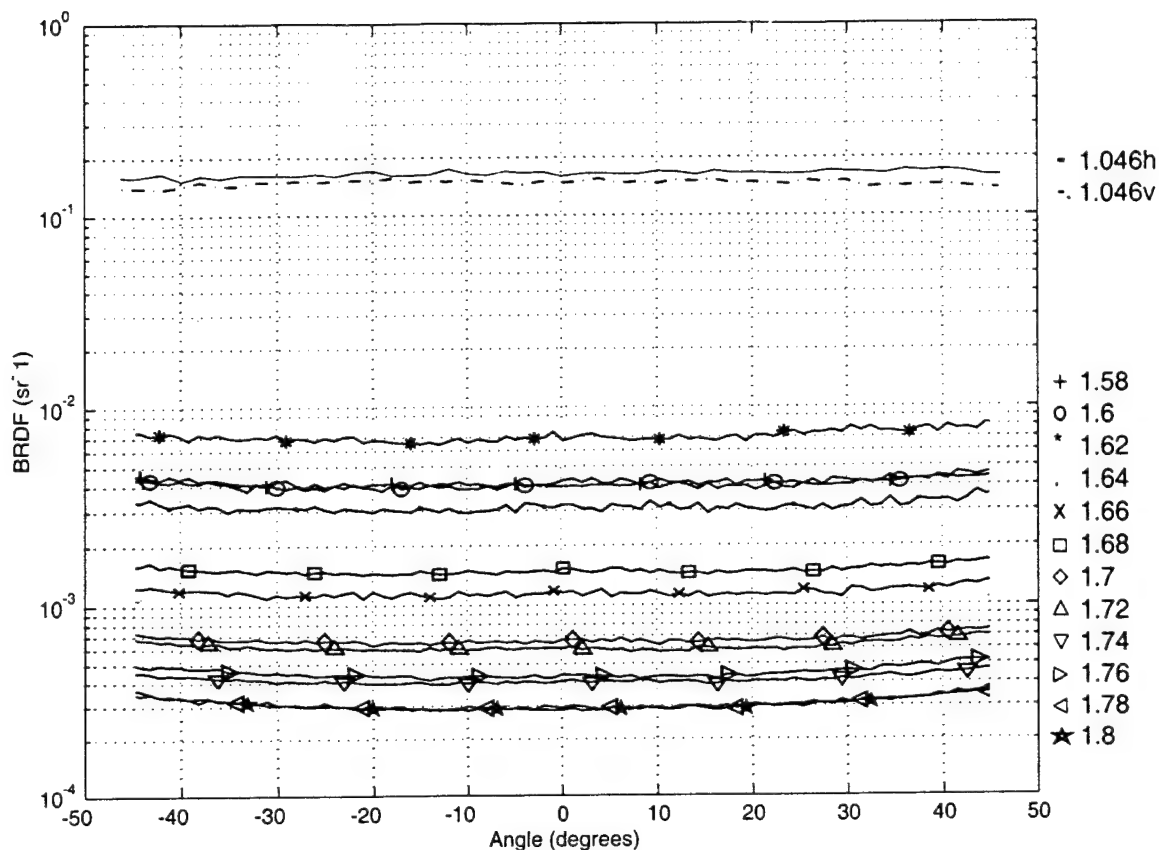
Figure 20 - Bistatic BRDF for Green CARC Paint Using Silicon Photodiodes

Since the beamsplitter is removed in the bistatic configuration, measurements for the vertical component were also collected. There was no polarization selection process on the reflected energy due to the silicon detector's low responsivity at $1\mu m$ and the wideband polarizer's low transmission coefficient.

Both polarizations maintained a BRDF mean near .3095, which corresponds to a 97% Lambertian reflector. A .54% separation between the vertical and horizontal components can be attributed to precision in the system calibration factor and the characterization of the CaF_2 reference detector pickoff, since these are calculated separately for each polarization.

46

4.2 General System Errors

This section addresses the errors associated with the individual components of the systems presented in Section 4.1. The discussion will follow the logical path from source to target detector. Recommendations will be provided in Chapter V.

The original intent of this research was to design and construct a BRDF measurement system capable of characterizing samples from a -45° to +45° angle of incidence over a 1.0μm - 5.0μm range. Additional research involved varying the incident polarization and observing the depolarization effects of materials.

4.2.1 Tunable Source

The Q-Peak LADAR, on loan from AFRL/MN at Eglin AFB, FL, was designed to produce a 1.5μm - 1.7μm signal beam and a 2.0μm - 2.4μm idler beam at 300mW continuous and 6kW peak pulse power at a 10kHz pulse repetition frequency. The system passed all functional tests at the AFRL/MN laser testing facility and was transported via government vehicle to building 194 for integration into the BRDF system. Initial testing on site showed limited output power (~ 100mW continuous) and severe fluctuations believed to be caused by the temperature controlled second harmonic generator. Optimal temperature settings for this device varied on a daily basis and required continual monitoring and adjustment.

Following a power disconnect caused by a faulty or overloaded power strip, measured power was reduced to zero at the output aperture. Slightly below threshold power was measured at the input to the RTA cavity preventing it from lasing. An

upstream adjustment/alignment approach was taken to increase this power. After determining the optimal pump current level and SHG temperature, alignments were made to the 523nm turning mirrors to center the beam on the downstream optics. This further required the adjustment of the Ti:S cavity mirrors. This effort was insufficient to bring the Ti:S output to above the RTA threshold. A decision was then made to power down the system and clean the optics, in an effort to reduce Rayleigh scattering, using compressed air. A subsequent power up yielded a Ti:S output power of zero. A full system realignment was then accomplished with the manufacturer's guidance; however, the complexity of the Ti:S cavity impeded and eventually terminated the effort. To this point, the Nd:YLF cavity had produced 1.046μm light without equivocation; therefore, the tunable LADAR system was dismantled and used as a discrete source.

4.2.2 ½-Wave Plate and Polarizing Beamsplitter

These two components work collectively to select the linear polarization component desired at the target. Varying the polarization is also required in order to characterize the beamsplitter, since certain samples are expected to depolarize the signal. Unfortunately, these components vary with wavelength and none were available at 1.046μm. However, no such shortage exists at the Nd:YAG 1.06μm wavelength. These slightly unmatched components were expected to function adequately, assuming the material indices had small or no wavelength dependencies.

Another uncertainty in polarization selection efficiency exists due to alignment of the polarizing beamsplitter. This device uses Brewster's angle to theoretically pass all of the in-plane (p-polarization) component and reflect a large portion of the out-of-plane (s-

polarization) component. If this device is not aligned properly, the polarization efficiency decreases. Alignment was particularly difficult, due to the mount used, when selecting the horizontal polarization.

4.2.3 CaF$_2$ Telescope

The 4 times CaF$_2$ telescope is integrated into the system to expand and collimate the beam. The light incident upon the target must be collimated in order to accurately characterize any surface and expansion of the beam reduces speckle size. The telescope is placed upstream from the reference detector branch, making characterization of the optics unnecessary. Careful attention is placed on centering the beam throughout the telescope in order to maintain collimation and the desired path. Unfortunately, the expanded beam was observed to be nonuniform and the afocal configuration of the telescope prevented placement of a spatial filter between the lenses to filter out the higher order TEM modes. Consequently, an iris was placed at the output in order to select a portion of the signal with uniform appearance. This reduced beam expansion considerably and nearly returned calculated speckle to its original size.

4.2.4 CaF$_2$ 50/50 Beamsplitter

With exception to the source, the CaF$_2$ beamsplitter was the most difficult to characterize and the most limiting component in the system. As mentioned previously, two spots were observed in the target branch of the system during the alignment process. Two spots were also observed at the target when the $\frac{1}{2}$-wave plate and polarizing

49
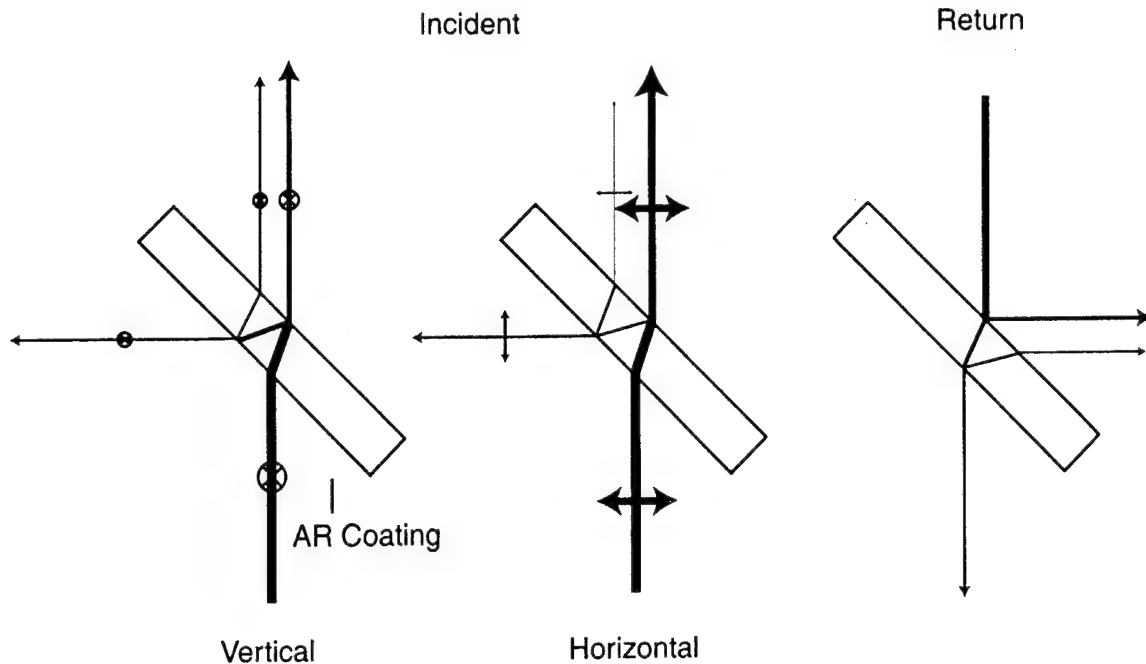
Figure 21 – Light Propagation Through CaF$_2$ 50/50 Beamsplitter

beamsplitter were adjusted to select the vertical (s-polarization) component. Figure 21 graphically describes the source of these errors.

Brewster's angle for the CaF$_2$ substrate (assuming n = 1.399) is 54.4° and the orientation of the beamsplitter places the incident light at 45°. This combines to significantly reduce any internal back reflection for the horizontal case. While the reflected in-plane polarization component decreases as the angle of incidence approaches Brewster's angle, the reflected portion of the out-of-plane polarization component increases exponentially near and beyond this angle.

The front surface (facing the source) of the beamsplitter is anti-reflection (AR) coated to reduce losses while the back surface provides the 50/50 split. The coating was designed for, but not limited to, the 3μm - 5μm band. A reflection from the coated surface was not observed and is believed to be the result of the following relationship

$$d = \frac{\lambda_c}{4} = \frac{(2n+1)\lambda_s}{4} \qquad\qquad (10)$$

where d is the thickness of the coating layer at a 45° angle of incidence, λ_c is the wavelength for which the particular layer was designed, and λ_s is the wavelength of the light incident upon that coating. In this case, by setting $n = 1$ and $\lambda_s = 1.046\mu m$, we find that $\lambda_c = 3.138\mu m$. This obviously falls within the specified $3\mu m$ - $5\mu m$ band and, assuming that the beamsplitter is properly oriented and one of the discrete layers meets this condition, no front surface reflection should be observed.

Unfortunately, the back surface is not coated and reflects a portion of the beam onto the backside of the AR coated (front) surface; this beam is no longer incident upon the coated surface at 45°. In fact, the angle approaches 30° (using Snell's Law and the law of reflection), thus shifting the AR band left. Also, the wavelength within the CaF_2 substrate equals the free space wavelength divided by the substrate index of refraction (or 747nm). The new internal wavelength did not appear to match the conditions of Equation (10).

The target branch and beamsplitter may be aligned such that the two spots diverge sufficiently to select the desired front surface reflection and dump that of the back surface. However, this is only true for the specular case. In the case of a diffuse reflector, the two surface reflections cannot be separated and must be included when characterizing the beamsplitter. This presents problems when attempting to characterize materials that are completely or partially specular.

Another option is to combine the two surface reflections by reducing the beamsplitter's angle of orientation. The two spots became indistinguishable near 20°; however, the signal at the target detector was too weak to detect. This is expected, according to the Fresnel Equations, since the reflectance of any material is reduced as the angle of incidence is decreased.

A 70/30 ZeSe beamsplitter was also tested and the spot separation increased in all cases. This is expected since the thickness of this component is larger than that of the CaF_2 beamsplitter. Spot intensities also varied as a result of a higher index of refraction (n ≈ 2.4) and Brewster's angle ($\theta_p = 67.4°$).

4.2.5 Lambertian Calibration Standard

The Labsphere Spectralon SRS-99-020 99% Lambertian reflector was used to calibrate and verify all of the BRDF measurement systems described in Section 4.1. This sample is accompanied by a calibration certificate, which provides statistics and the methods used for verification. The random uncertainty, expressed by standard deviation, of reflectance measurements performed by Labsphere, Inc. on this particular sample is less than or equal to 0.020 over the spectral range 250-2500nm. The method used to collect the data and produce this statistic involves measuring the reflectance using a PerkinElmer Lambda 9 double beam ratio recording spectrophotometer equipped with a Labsphere integrating sphere accessory. Incident flux at 8° from normal is reflected from the sample onto the internal surface of the integrating sphere and compared to a laboratory working standard [24].

Limiting the angle of incidence to 8° does not adequately characterize the material, thus its use for BRDF calibration is suspect. In fact, this method measures the directional hemispherical reflectance (DHR) of the surface, which is defined as the ratio of the total power reflected by a surface (into the hemisphere) to the power incident upon it [1]. Conversely, the 2.7% standard deviation error measured in Case 5 is closely matched to the 2.0% listed in the calibration certificate.

4.2.6 Miscellaneous

Other concerns regarding equipment used were notable, but less prominent than those listed in the previous sections. For instance, the iris used to stop down the beam after expansion and collimation is believed to be responsible for the circular aperture induced Fresnel Rings that were observed downstream. However, this ringing was inconsequential in comparison to the nonuniformity of the expanded beam caused by higher order transverse electromagnetic modes.

Uncertainties were also associated with the use of focusing lenses. Due to the ringing caused by the iris and the relatively large spot size of the beam (when compared to detector active area), a lens was necessary to ensure that all, or at least the majority, of the energy was focused onto the active area of the reference detector. Prior to focusing the energy in the reference branch, the detector was aligned to maximize the measured voltage output. This dictates that the beam must maintain an energy distribution that is constant in time regardless of its spatial nonuniformity. Measurements in this configuration were unstable and thus discarded.

A focusing lens is also placed before the wideband polarizer in the monostatic configuration in order to reduce speckle, by maintaining the target to detector distance while increasing the effective active area of the detector. This effort was moderately successful in improving results. However, the integrity of the data collected is suspect by reason of uncertainties associated with calculation of the solid angle.

Assuming the reflected energy to be perfectly collimated, the lens (or polarizer input aperture in this case) defines the area and distance from the target used in calculating the solid angle. As mentioned previously, this assumption can only be applied to a perfectly specular target and not to a diffuse reflector which reflects energy in all directions. A sufficiently large detector will reduce this uncertainty. Additionally, such a detector may not require a lens simply to defeat the effects of speckle. Determining an accurate solid angle model as a function of target properties is beyond the scope of this experiment, thus the lens is removed from the target branch.

V. Conclusion and Recommendations

This chapter presents the conclusions reached regarding the systems and components described in Chapters III and IV as well as recommendations for future research in this area.

5.1 Conclusions

A monostatic BRDF measurement system was developed based on recommendations from prior research. Slight modifications were made in an effort to improve the quality and utility of the collected data, but unacceptable results were achieved. This may be primarily attributed to the reduced solid angles associated with increased target to target detector separation forced by the required wideband polarizer and the uncertainties associated with characterization of the beamsplitter in this configuration. Table 3 summarizes the results obtained for the 99% Lambertian standard in the monostatic arrangement.

Table 3 – 99% Lambertian Monostatic BRDF Results

Input Polarization[10]	Reference Detector	Target Detector	Reference Lens	Target Lens	Wideband Polarizer	Beamsplitter	Error
Horizontal (p)	InSb 500μm	InSb 250μm	Y	Y	Y	CaF$_2$	11.7%
Horizontal (p)	InSb 500μm	InSb 250μm	Y	Y	Y	ZeSe	14.0%
Horizontal (p)	InSb 500μm	InSb 250μm	Y	Y	N	CaF$_2$	10.9%
Horizontal (p)	InSb 250μm	InSb 500μm	Y	N	N	CaF$_2$	36.3%

---

[10] Input polarizations were limited to horizontal in the monostatic configuration due to the observation of multiple spots at the target for vertical polarization (see Figure 21).

These results indicate that the errors are predominantly equipment and not target related, assuming that the specified error of ≤ 2% associated with the Lambertian standard is accurate. Many of the missing configurations were initiated and soon aborted due to obvious fluctuations in signal level at the target detector. The silicon photodiodes are not represented as a result of insufficient responsivities leading to minimal detection of the reflected energy in this configuration.

Table 4 summarizes the errors associated with the bistatic configuration. No data shifting or cropping was used to produce the results in either table.

Table 4 - 99% Lambertian Bistatic BRDF Results

Input Polarization	Reference Detector	Target Detector	Reference Lens	Target Lens	Wideband Polarizer	Beamsplitter	Error
Horizontal (p)	InSb 500μm	InSb 250μm	Y	N	N	None	10.9%
Horizontal (p)	Si 282μm	Si 282μm	Y	N	N	None	6.4%
Vertical (s)	Si 282μm	Si 282μm	Y	N	N	None	5.5%

The presented statistics clearly indicate that the bistatic configuration outperforms the monostatic system regardless of the detector used. However, the observed benefit is grossly underestimated given the diffuse nature of the target being characterized. In the monostatic configuration, characterization of diffuse materials is achievable since the system is calibrated using a diffuse standard. The beamsplitter may be sufficiently characterized for the diffuse case since energy from both surfaces are scattered in all directions and reach the detector. The beamsplitter can also be separately characterized for purely specular targets; however, this is impossible for samples with both specular and diffuse properties.

5.2 Recommendations

This section will offer recommendations for improvements in equipment and configuration which can be used in follow-on research. Acquiring this equipment may take longer than the setup, calibration, and data collection phases combined. Therefore, the serious student should be more proactive than reactive and determine the availability of the suggested equipment long before dedicating themselves to follow-on research in this area.

A source, entirely or partially tunable across the desired $1.0\mu m$ - $5.0\mu m$ band, with a near Gaussian energy distribution (TEM_{00}) is desired. A q-switched laser removes the requirement for a chopper wheel and lock-in amplifier provided that the q-switch pulse is used to trigger the oscilloscope. Excessive linewidth and multiple spectral lines should be avoided since many components exhibit nonlinear spectral properties. A monochromator may be used to remove unwanted lines and reduce linewidth. However, the typical monochromator, including the Acton Research Corporation SpectraPro – 275 triple grating monochromator used in this research, has a low energy damage threshold.

The ½-wave plate and polarizing beamsplitter used in this experiment were specifically designed to operate at or near $1.06\mu m$. These components were sufficient in this case, given the source limitations, but inadequate to efficiently select polarizations across the desired band. A tunable ½-wave plate and linear polarizer are preferred and the Cleveland Crystals Inc. IR-1600 polarizer meets specifications. Unfortunately, tunable wave plates are scarce and even more difficult to operate. The Cleveland Crystals model XPT tilt-tunable wave plate illustrates this point by being removed from production, citing the lack of consumer ability to operate the device. On the other hand, the wave plate may

not be necessary, provided the source exhibits sufficient components of both linear polarizations or is capable of being physically rotated to do so. This allows the wideband polarizer to be used autonomously to select the desired polarization. A computer controlled apertured rotation stage can be used to automatically and precisely select the polarization; this is also the case for the wideband polarizer associated with the target detector.

The variable neutral density filter is critical in determining the range of targets for which the system is capable of reliably collecting data. Although not required, it should be spectrally flat across the desired band. The BK7 material in the typical variable ND filter demonstrates a nearly ideal transmission curve between 400nm and 2.0µm, but begins to absorb sharply thereafter; this is also true for the focusing lens in the reference branch. Locating a variable filter that extends into the mid-IR may be as futile as the variable ½-wave plate; however, a CaF_2 (or similar material) window may be placed at this point in the system and rotated about its vertical or horizontal (perpendicular to propagation) axis (depending upon polarization) in order to vary the transmission through the device. The thickness of the window should be minimized to prevent translation of the beam.

The CaF_2 telescope with 4 times magnification was crucial to ensure that the beam incident upon the target was both collimated and sufficiently large in spot size. Unfortunately, the beam exhibited nonuniform properties and had to be stopped down to select a more homogeneous portion of the beam. This resulted in circular aperture induced Fresnel Rings, which may have corrupted measurements by the reference and target detectors. Placing a spatial filter within the telescope and removing the iris may reduce

this ringing[11]. It is also possible that the reference detector CaF_2 pickoff induced Haidinger Fringes, which are fringes of equal inclination induced by thick plates [14].

The CaF_2 50/50 beamsplitter is not believed to have contributed an appreciable amount to the errors observed, since only diffuse materials were characterized. If a monostatic configuration is preferred, the beamsplitter should be sufficiently thin so as not to alter the beam's energy distribution at the target or at the target detector. The window should be anti-reflection coated on both surfaces to prevent excessive loss at the front surface and to further assure that multiple reflections are not observed in the target branch.

Another solution is to take a bistatic approach, thereby removing any uncertainties associated with the beamsplitter. The angular range was limited due to the offset in positioning of the target detector; however, this may be overcome by suspending the detector over the target in line with the propagation axis. Care must be taken to ensure that the line extended between the center of the spot on the target and the detector's active area is normal to that surface. This is necessary to guarantee the accuracy of the solid angle. The change in surface area of the target as seen by the detector and the resulting falloff in intensity must also be calibrated by placing a $\cos(\phi)$ into the denominator of Equation (2), where ϕ is the angle between the incident light propagation axis and the line normal to the detector's active surface.

Nonuniformities in scatter due to material surface defects and speckle effect are difficult to characterize or isolate. One method of reducing the variations associated with these properties is to rotate the sample about the axis defined by the target surface normal. This should average out any speckle/spatial variations in the reflected energy [29].

---

[11] Both lenses must be positive to produce a real focal point within the telescope.

Another option is to select a detector with a larger active area. The silicon photodiodes provided more reliable measurements than the InSb detectors due in part to their increased active surface area. However, surface area alone does not adequately define the capabilities of a detector. The NEP of the silicon detector is also two orders of magnitude lower than either of the InSb detectors, but the peak responsivity is also one order less. Consideration must also be given to calculation of the BRDF when selecting the appropriate aperture size and consequent solid angle. Equation (2) assumes the power on the active surface of the detector to be uniform, thus allowing the reduction of the BRDF from differential to absolute form. As solid angles increase, use of this assumption becomes increasingly ambiguous.

The PerkinElmer J10D-M204-R07M InSb photovoltaic detector boasts properties that can be expected to produce results that are far superior to those obtained in this research. The 7mm active diameter provides a 19,500% increase in active area with only a 1,400% increase in NEP[12].

These system modifications should easily reduce, if not remove, the errors encountered in this experiment. Once implemented, this multispectral BRDF system can be used to build a highly spectral database of diverse materials. A word of caution should follow these recommendations, since all component and material characterizations were restricted to a discrete wavelength. All of the components recommended are designed to operate with near linear properties across the $1.0\mu m - 5.0\mu m$ band; however, they are not immune to errors resulting from spectrally variant conditions like etalon effect.

---

[12] Compared to the 500μm active diameter J10D InSb detector.

Additional research is warranted in the area of band optimization. Following the completion of BRDF measurements, materials may be classified in order to reduce the number of discrete sources or the tunable range required for operational systems. Multiple techniques have been developed including: principle component analysis (PCA), multiband signal to clutter ratio (SCR), correlation band selection algorithm (CBAND); refer to (appendix) Section B.1.1 for more information on analytic and empirical band selection techniques. Atmospheric absorption should also be considered in the band optimization process prior to laboratory data collection.

Appendix A. Matlab Code for BRDF Calculation

```
% Written to graph BRDF data based on the following inputs:
% Input Power (incident_pwr)
% Reflected Power (reflected_pwr)
% Solid Angle subtended by target receiver (solid_angle)
% Rotation Stage Position (stage_position)

This file corresponds to a fixed wavelength (1.046µm)

clear all
format long;

%load generic data files/input variables

wavelength=1046;%in nanometers used for responsivity curve
caf2_po_tr_ratio=92;%reference detector pickoff transmission to
                    %reflection ratio
ref_det_att=.001;%OD 3.0 neutral density filter for reference detector
tar_det_aperture=282*10^-6;%radius of Si target detector aperture in
                           %meters
target_distance=.092075;%distance from target to target detector
system_cal=.8605;%overall system cal found using 99% Lambertian target
                 %must be set to 1.0 to determine precalibrated mean
                 %.99*(1/pi) is then divided by the brdf mean to get
                 %this calibration factor

%solid angle defined by the target detector active area and target %to
target detector distance
solid_angle=(pi*(tar_det_aperture)^2)/(target_distance)^2;

%load data files for reference and target detectors separate matrices for
each using loadfiles.m
loadfiles_1046_199h_si;

%cycle through the detector matrices as a function of angle
for m=1:47;%begin stage/target position loop
stage_position=(-48+2*m)*pi/180;%stage position from -46 to 46 deg
                                %converted to rads in 2 deg increments
   ref_time=ref_fe_mat(:,2*m-1)*10^6;%time vector for reference detector
   ref_magnitude=ref_fe_mat(:,2*m);%magnitude vector for reference
                                   %detector
   tar_time=tar_fe_mat(:,2*m-1)*10^6;%time vector for target detector
   tar_magnitude=tar_fe_mat(:,2*m);%magnitude vector for target detector

%load data files/input variables for reference detector
load ref_curve.txt;%reference detector spectral responsivity curve
%ref_ti=10^7;%V/A selectable transimpedance gain for reference preamp
            %not used with silicon detectors
ref_res_pk=0.4;%A/W relative peak responsivity

%load data files/input variables for target detector
load tar_curve.txt;%target detector responsivity curve
%tar_ti=10^7;%V/A selectable transimpedance gain
            %not used with silicon detectors
tar_res_pk=0.4;%A/W relative peak responsivity/see spreadsheet
```

```
%determining peak reference detector power

%vector of wavelegths from responsivity curve for ref det
ref_wave_vec=ref_curve(:,1);

%normalized vector of wavelegths from responsivity curve for ref det
norm_ref_wave_vec=abs(ref_wave_vec-wavelength);

%locate nearest maching wavelength
norm_ref_wave_min=min(norm_ref_wave_vec);

%find index of matching wavelength
wave_vec_index=find(norm_ref_wave_vec==norm_ref_wave_min);

%find max value on responsivity curve for ref det
max_ref_curve=max(ref_curve(:,2));

%multiplier to normalize data for ref det
ref_multiplier=ref_res_pk/max_ref_curve;

%index for matching wavelength for ref det
true_val_index_ref=wave_vec_index;

%actual non-normalized value for ref det
true_val_ref=ref_curve(true_val_index_ref,2);

%normalized value of responsivity for ref det
ref_res=ref_multiplier*true_val_ref;

%voltage responsivity of detector
ref_vw=ref_res%*ref_ti;%volts/watt for ref det

%maximum voltage value of collected data for ref det
ref_roof_volt=max(ref_magnitude);

%maximum power value of collected data for ref det
ref_roof_pwr=ref_roof_volt/ref_vw;

%finds time and index near zero seconds which is a good point before the
%rise
[r,index]=min(abs(ref_time));

%take average from first point to point before rise

%minimum voltage value of collected data for ref det
ref_floor_volt=mean(ref_magnitude(1:index));

%minimum power value of collected data for ref det
ref_floor_pwr=ref_floor_volt/ref_vw;

%peak power for ref det
ref_pk_pwr(m)=ref_roof_pwr-ref_floor_pwr;


%determing peak target detector power

%vector of wavelegths from responsivity curve for tar det
tar_wave_vec=tar_curve(:,1);
```

```matlab
%normalized vector of wavelegths from responsivity curve for tar det
norm_tar_wave_vec=abs(tar_wave_vec-wavelength);

%locate nearest maching wavelength
norm_tar_wave_min=min(norm_tar_wave_vec);

%find index of matching wavelength
wave_vec_index2=find(norm_tar_wave_vec==norm_tar_wave_min);

%find max value on responsivity curve for tar det
max_tar_curve=max(tar_curve(:,2));

%multiplier to normalize data for tar det
tar_multiplier=tar_res_pk/max_tar_curve;

%index for matching wavelength for tar det
true_val_index_tar=wave_vec_index2;

%actual non-normalized value for tar det
true_val_tar=tar_curve(true_val_index_tar,2);

%normalized value of responsivity for tar det
tar_res=tar_multiplier*true_val_tar;

%volts/watt for tar det
tar_vw=tar_res%*tar_ti;

%maximum voltage value of collected data for tar det
tar_roof_volt=max(tar_magnitude);

%maximum power value of collected data for tar det
tar_roof_pwr=tar_roof_volt/tar_vw;

%take average from first point to point before rise

%minimum voltage value of collected data for tar det
tar_floor_volt=mean(tar_magnitude(1:index));

%minimum power value of collected data for tar det
tar_floor_pwr=tar_floor_volt/tar_vw;

%peak power for tar det
tar_pk_pwr(m)=tar_roof_pwr-tar_floor_pwr;


%Calculate incident power
incident_pwr(m)=caf2_po_tr_ratio*(ref_pk_pwr(m)/ref_det_att);

%Calculate reflected power
reflected_pwr(m)=tar_pk_pwr(m);

%Calculate BRDF
brdf(m)=system_cal*(reflected_pwr(m)/solid_angle)/(incident_pwr(m)*cos(st
age_position));

%used for plots
stg_pos(m)=-48+2*m;
cosine(m)=cos(stg_pos(m)*pi/180);
end%end stage/target position loop
```

```
%BRDF Statistics
brdf_std_dev=std(brdf)
brdf_mean=mean(brdf)
error_percentage=brdf_std_dev/brdf_mean
ref_mean=mean(ref_pk_pwr)
ref_std_dev=std(ref_pk_pwr)
ref_error=ref_std_dev/ref_mean


% Pulse Plots
figure(1)
subplot(2,1,1)
plot(ref_time,ref_magnitude,'b.');
title('Figure 1: Reference Pulse at 1.046 {\mu}m');
ylabel('Pulse Amplitude (Volts)');
xlabel('Time (us)');
grid on;

subplot(2,1,2)
plot(tar_time,tar_magnitude,'b.');
title('Figure 2: Target Pulse at 1.046 {\mu}m');
ylabel('Pulse Amplitude(Volts)');
xlabel('Time (us)');
grid on;

%BRDF Plot
figure(2)
semilogy(stg_pos,brdf,'b');
title('Figure 3: 99% Lambertian BRDF 1.046{\mu}m vs Target Angle');
ylabel('BRDF (sr{^-1})');
xlabel('Angle (degrees)');
grid on;
ylim([10^-2 10^0]);

%Target Detector Power Plot
figure(3)
plot(stg_pos,tar_pk_pwr*1.5E8,'r');hold on
plot(stg_pos,ref_pk_pwr*1.7E8,'g');hold on
plot(stg_pos,cosine,'b');
title('Figure 4: 99% Lambertian Measured Power 1.046{\mu}m vs Target
Angle');
ylabel('Normalized Power');
xlabel('Angle (degrees)');
legend('Target Power','Reference Power','Cosine')
grid on;
```

Appendix B. Band Optimization

This section addresses several band selection techniques and the interaction between electro-magnetic radiation and the atmosphere. Atmospheric absorption and emission severely affect the performance of electro-optical systems and should consequently be considered in the development process; this is also true in the case of material classification. Laboratory BRDF measurement systems are less susceptible to atmospheric attenuation since path lengths are typically restricted between the target material and the detector measuring the reflected power. However, atmospheric phenomena must be considered in the band selection process and should be involved in the material characterization process in order to reduce unnecessary measurements and time required.

B.1 Multispectral Band Selection

The number of available spectral bands in multispectral systems is limited by multiple constraints; this is particularly true in operational systems. In a laboratory environment, these bands are typically constrained only by the optical components, detectors, and the source. In an operational system, further restrictions include weight, size, and ruggedness. Current technological limitations prevent the integration of a source that is completely tunable across the desired $1\mu m$ - $5\mu m$ region and size and cost preclude incorporating multiple discrete sources.

Previous research suggests that detection performance increases asymptotically with the number of spectral bands incorporated [22]. That is, the addition of bands provides an increasingly smaller gain in system performance, thereby reducing the

necessity of a continuously tunable source when attempting to characterize a particular class of materials (for operational systems).

B.1.1 Band Selection Techniques

Prior to band optimization, data must be collected across the entire spectral region of interest. Post collection processing is then accomplished in order to classify materials using a specified number of spectral bands. Multiple techniques are available and will be introduced with varying levels of discussion.

B.1.1.1 Principal Component Analysis

One such technique is called principal component analysis (PCA). This method uses classical statistical methods to determine bands with maximum decorrelation and is widely used in multispectral and hyperspectral data analysis. One subset of this method is the modified stepwise PCA (MSPCA), which addresses the importance of each of the original bands in each resultant feature (i.e. the eigenvectors). This approach optimizes these features in the sense that the number of features can be substantially smaller than the original quantity of bands without a significant loss of information in terms of proportion of variance [7]. A principal component in its most primitive form can be given as

$$PC = Xb \qquad (11)$$

where PC is the elemental measurement vector, b is the variable (or band in this case) vector, and X is a matrix defined in the following relationship

$$X'X = nR \qquad\qquad (12)$$

where n is the number of measurements and R is the correlation matrix. Following additional mathematical development, the PCA may be expressed in the eigen-value/eigenvector form

$$\left(B^{-1}W - LI\right)c = 0 \qquad\qquad (13)$$

where W and B correspond to the within-class and between-class variances, respectively. L and c are the eigenvalue and eigenvector of the quantity $B^{-1}W$, respectively.

The PCA organizes the linear combinations of the original measurements according to eigenvalues. In contradiction to the general strategy, the first criterion to be considered recognizes the feature accounting for the smallest variance, which corresponds to the smallest eigenvalue. The band with the largest weight (or coordinate value in the eigenvector) associated with the smallest eigenvalue is considered the noisiest and can be removed from the solution set. Once this band is removed, the iterative process begins again in determining the smallest eigenvalue and then the largest associated eigenvector coordinate value and so on. These iterations continue until the desired number of bands remains.

B.1.1.2 Signal-to-Clutter Ratio

Multi-band signal-to-clutter ratio (SCR) is a target and band selection technique based upon the generalized signal-to-noise ratio. The SCR is a normalized metric that quantifies the separation in N-dimensional space of a target mean from a background mean

relative to the variation of the background distribution. For a single band passive sensing system, the SCR is simply the difference between the target and background mean radiance normalized by the standard deviation of the background [23]. This can also be applied to an active system where the SCR is computed using a set of independent spectral measurements, such as reflectance or BRDF. In this case, the noise or background measurements may be substituted with measurements from another material class or atmospheric absorption spectra. In all scenarios the N-dimensional SCR metric is defined by

$$SCR = \sqrt{b^T M^{-1} b} \tag{14}$$

where b is the mean difference vector between the target and background or a set of classes and M is the background (or class) covariance matrix. In the 2-dimensional case, the SCR takes the form

$$SCR = SCR_1 \left[\left(1-\rho^2\right)^{-1} \left(1-2\rho R + R^2\right) \right]^{1/2} \tag{15}$$

Where SCR_1 is the signal-to-clutter ratio associated with the two-band case, ρ is a band-to-band spectral correlation coefficient, and R is the color ratio (or ratio of SCRs for the two bands of interest) [27].

B.1.1.3 Class Separability

Another method uses a class separability metric based on the within-class and between-class scatter matrices. In order to maximize the performance of the band

optimization algorithm and the material classification system, the probability of error for the selected classifier and observation model must be minimized. In a two-class system with Gaussian power density functions, computing the probability of error is unwieldy and is usually replaced by applying a bound metric such as the Bhattacharyya bound [13]. In multi-class scenarios, no such bound exists and forces the use of a more practical approach, such as the aforementioned class separability matrix.

By assuming the existence of L classes of materials and that the only variations in the associated observations stems from differing object reflectivity spectrums, the within-class scatter matrix may be defined as

$$S_w = \sum_{k=1}^{L} P_k C_{xk} \tag{16}$$

where P_k is the a priori probability of observing class k, and C_{xk} is the covariance for the observation class k. The between-class scatter matrix measures the scatter of the mean vectors as

$$S_b = \sum_{k=1}^{L} P_k \left(z_k - \bar{z} \right) \left(z_k - \bar{z} \right)^T \tag{17}$$

where

$$\bar{z} = \sum_{k=1}^{L} P_k z_k \tag{18}$$

is the mean vector of the mixture distribution and

$$z_k = \left[z_{k,1}, z_{k,2}, \ldots, z_{k,n} \right]^T \tag{19}$$

defines the noise and speckle free optical return power for class k. The resulting metric used as a measure of class separability is then

$$J = tr\left(S_w^{-1} S_b \right) \tag{20}$$

where $tr(\cdot)$ represents the trace operation [13]. Large values of J indicate large between-class scatter separation relative to within-class scatter. This is the desired result and is more easily addressed in the following example where J is essentially the separation in class reflectance values for a given spectral band.

Consider the case of three material classes and two spectral bands. In this scenario, the separability metric is defined as

$$J = \sqrt{\left(x_1 - y_1 \right)^2 + \left(x_2 - y_2 \right)^2} + \sqrt{\left(x_1 - z_1 \right)^2 + \left(x_2 - z_2 \right)^2} + \sqrt{\left(y_1 - z_1 \right)^2 + \left(y_2 - z_2 \right)^2} \tag{21}$$

where x_i, y_i, and z_i represent the material class reflectance values and i indicates the spectral band. In the 1-dimensional (single band) case, the optimization algorithm maximizes J by maximizing the between-class scatter (or separation of reflectance values) for classes x and y, x and z, and y and z. In the 2-dimensional case, the algorithm first maximizes J in 1-dimensional space and then iteratively searches the remaining available bands to maximize J in the 2nd dimension. This process is repeated until the desired number of bands is reached.
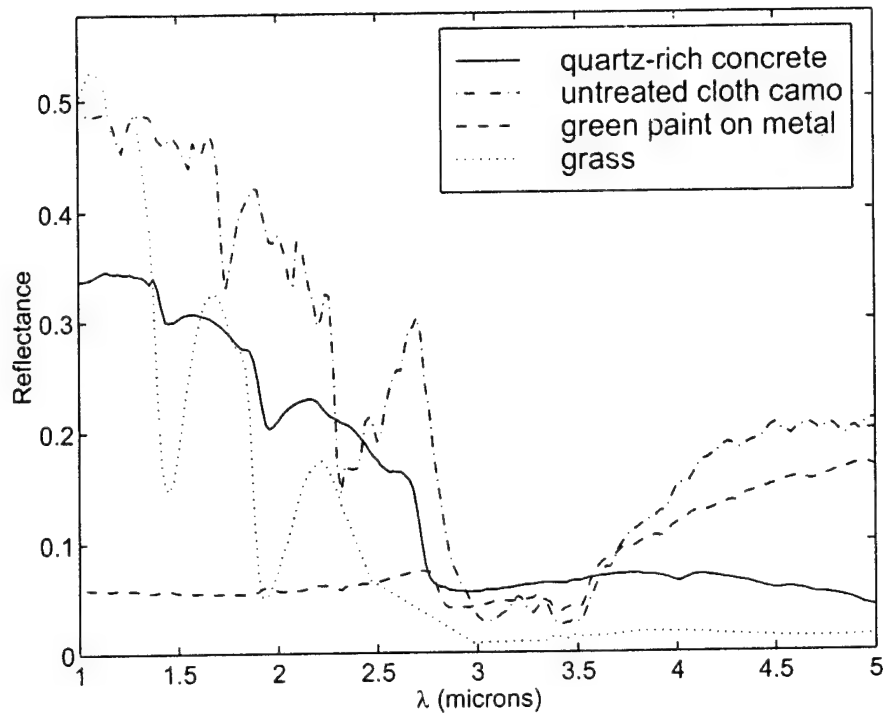
Figure 22 – Reflectance Spectra for a Sample Set of Material Classes

B.1.1.4 Correlation Band Selection

The final band selection technique to be discussed is the correlation band selection algorithm (CBand). This method attempts to identify optimal bands by directly comparing the reflectance spectra for material classes or comparing reflectance data of some unclassified material with those of a classified set. This is particularly useful when attempting to extract a target from a known background. Figure 22 introduces reflectance spectra for typical background classes and highlights the spectral variations between these classes.

In the two-band two-class case, the desired result produces an order-of-magnitude exchange in reflectances. In other words, class 1 may have a large reflectance value in band 1 and a small reflectance in band 2, while the opposite is true for class 2. For

instance, visual inspection of Figure 22 indicates once such band near 1.9μm, when attempting to discriminate untreated cloth camouflage from grass. The second band, where these reflectance properties are inverted, exists near 1.7μm (subsequent to a normalization of the spectra). This is more quantitatively accomplished by computing the normalized cross-correlation between all of the bands of (initial) interest. The normalization is necessary to include the bands in which all of the classes exhibit small reflectance values. Excluding this step would allow those bands with larger reflectances to overpower those with smaller values, thus potentially eliminating bands with desirable properties. The normalized cross-correlation is given by

$$C_{i,j} = \frac{1}{L} \sum_{k=1}^{L} X_{k,i} X_{k,j} \tag{22}$$

where X represents the normalized class reflectance data for class k in bands i and j and L is the number of classes. The lowest value within the $C_{i,j}$ matrix then defines the first pair of optimized bands. In the case where additional bands are desired, a new selection metric is introduced in order to minimize the cross-correlation or maximize the separation in 2-dimensional cross-correlation space between the new band and the optimized set as shown

$$D_j = \left[\sum_{i=1}^{l} \left(C_{bi,j} - C_{bi,bi} \right)^2 \right]^{1/2} \tag{23}$$

where b_i is the ith band of l previously selected bands, and $j = 1,2,\ldots,N$ where N is the total number of considered bands.

One important feature in the CBand selection algorithm is the integration of atmospheric attenuation effects. This model accounts for atmospheric molecular absorption and removes bands where the transmission coefficient falls below 10% [19].

B.2 Atmospheric Absorption

Considerable discussion regarding optical transmission through the atmosphere is warranted, given the extensive level of atmospheric absorption in various bands within the $1\mu m$ - $5\mu m$ region. A thorough discussion on atmospheric constituents and optical properties of the atmosphere is also provided.

The atmosphere can be considered as a gaseous blanket that provides a temperature-controlled environment for the earth and its inhabitants. It plays an integral role in the thermal equilibrium process, which equates the average solar radiation received by the earth to the average radiant energy escaping the earth into space. Absorption and emission of sunlight by the atmosphere is a temperature dependent process and thus adjusts itself (temperature) until the outflow of energy matches the inflow. In recent years, the increase in CO_2 concentrations has increased the level of atmospheric absorption, consequently decreasing the radiative transfer to space. This process is referred to as the greenhouse effect and it forces the equilibrium temperature of earth to increase, thereby altering earth's ecosystem.

Earth's atmosphere is composed of many constituents with varying characteristics of absorption, emission, and optical scatter. Variations in pressure, temperature, and concentrations cause significant fluctuations in these optical properties and present a

formative challenge in the development of a representative model. Furthermore, these constituents vary with geographical region in time, space, and altitude.

B.2.1 Atmospheric Constituents

Radiative absorption by molecules in a gaseous medium can be attributed to two processes:

1. Atomic absorption is caused by the transition of electrons in an atom, and usually requires a photon with an energy of a few electron volts. This generally occurs in the visible or UV region of the spectrum.

2. Molecular absorption is caused by the transition between electronic, vibrational, or rotational energy states of a gaseous molecule. It may also results from a combination of each of these state transitions [25].

Molecular absorption is dominant in the IR region and is composed of multiple bands which contain many closely spaced discrete spectral lines. These bands are attributed to the transitions between different vibrational energy levels within the same electronic state, whereas the discrete lines within these bands are due to molecular rotation.

Earth's gaseous constituents and their respective volumetric contents are provided in Table 5. While all of these gases may contribute to atmospheric absorption in some form or another, the following will be limited to those with substantial absorptive contributions in the $1\mu m$ - $5\mu m$ region. The two most important infrared absorbers in this band are CO_2 and H_2O. The mixing of CO_2 in the atmosphere is relatively constant and independent of altitude; however, average volume may vary geographically by as much as 50%. This is particularly evident when comparing a large industrial city to a forest during

Table 5 – Composition of Atmospheric Constituent Gases [25]

Constituent Gas	Content (% by volume)
H_2	78.084
O_2	20.9476
Ar	0.934
CO_2	3×10^{-2}
H_2O	10^{-5} to 10^{-2}
Ne	1.81×10^{-3}
He	5.2×10^{-4}
CH_4	2×10^{-4}
Kr	1.14×10^{-4}
H_2	5×10^{-5}
N_2O	$\approx 5 \times 10^{-5}$
CO	$\approx 7 \times 10^{-6}$
O_3	0 to 7×10^{-6}
NO_2	0 to 7×10^{-6}
NO	0 to 2×10^{-6}

daylight hours. Photosynthesis in vegetation causes a reduction in CO_2 concentrations while exhaust from the burning of fossil fuels increases this concentration.

Figure 23 illustrates the effects of atmospheric absorption on solar radiation. The shaded areas indicate absorption bands and are associated only with the in-atmosphere curve. Measurements at sea level are provided to show the largest contrast; as altitude increases, H_2O vapor content decreases and these absorption bands are reduced significantly. The dominant reasoning for this decrease in water vapor content with increasing altitude is the dependence of H_2O upon temperature. As temperature increases, the amount of H_2O vapor in the atmosphere increases exponentially. Also, the cooler temperatures of the stratosphere tend to prevent the vapor from escaping the troposphere and thus the majority of all cloud formations are found within the troposphere. The
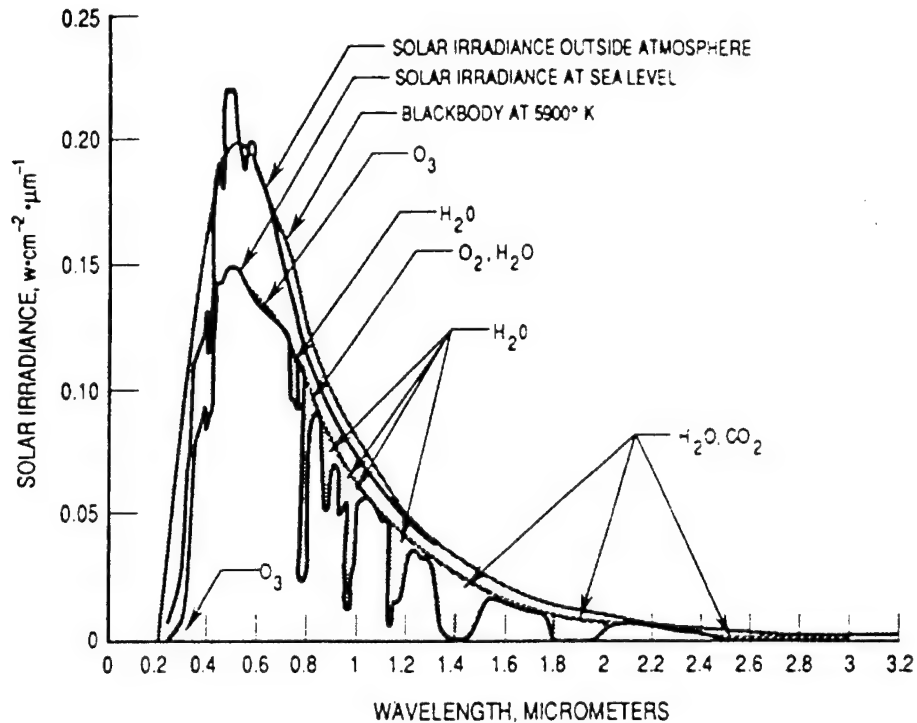
Figure 23 – Solar Spectral Irradiance at Earth's Surface and Outside Earth's Atmosphere (shaded areas indicate atmospheric constituent absorption)

highest measured H_2O content was measured at sea level and was approximately 30 grams (or 2 tablespoons) per cubic meter, which corresponds to nearly 3% of the atmospheric content by weight. The lowest atmospheric temperature of nearly -90°C is found in the stratosphere. Water vapor content at these temperatures is negligible and therefore makes no contribution to IR absorption. Figure 24 presents the major atmospheric constituents and their respective transmission spectra; the aggregate curve combines the averaged molecular absorptions into a single curve.

Due to the complex nature of heavy parametric absorption and its influence on radiometric measurements in the IR region, numerical analysis must be performed. Three widely used numerical methods are HITRAN (high resolution transmission), MODTRAN (moderate resolution transmission), and LOWTRAN (low resolution transmission).
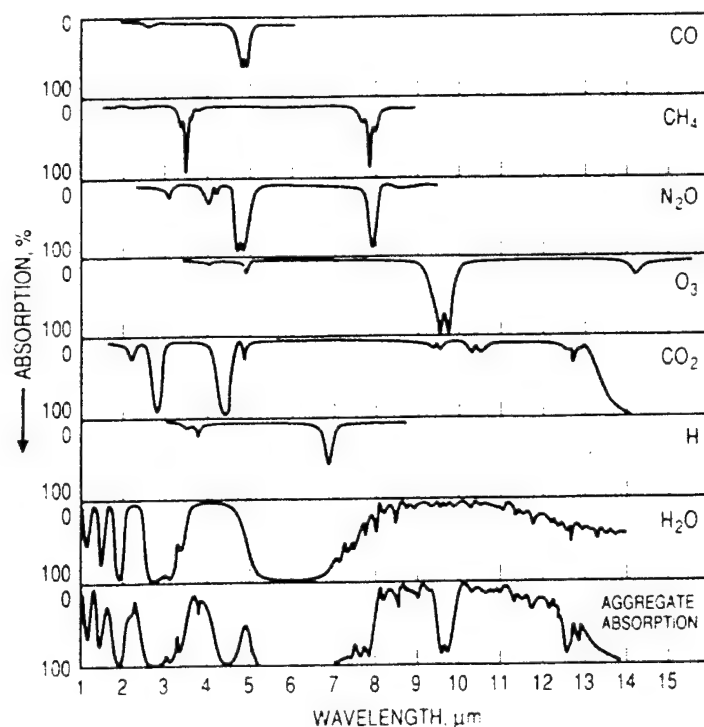
Figure 24 – Atmospheric Constituent and Aggregate Infrared Absorption

LOWTRAN code is a more efficient and flexible model for broadband systems; however, spatial resolution is limited to 20 cm^{-1}. Transmittance in these 20 cm^{-1} intervals is averaged as shown below

$$\overline{\tau}_{\Delta v}(\text{total}) = \overline{\tau}_{\Delta v}(\text{molecular line absorption})$$
$$\times \overline{\tau}_{\Delta v}(\text{molecular or Rayleigh scattering})$$
$$\times \overline{\tau}_{\Delta v}(\text{molecular continuum absorption}) \qquad (24)$$
$$\times \overline{\tau}_{\Delta v}(\text{aerosol extinction})$$

The aggregate absorption curve displayed in Figure 24 is a prime example of the broadband resolution of the LOWTRAN model.

MODTRAN increases the spectral resolution to 2 cm^{-1} while maintaining the majority of LOWTRAN's features; these include spherical refractive geometry, solar and lunar source functions, scattering (Rayleigh, Mie, single and multiple), and default profiles
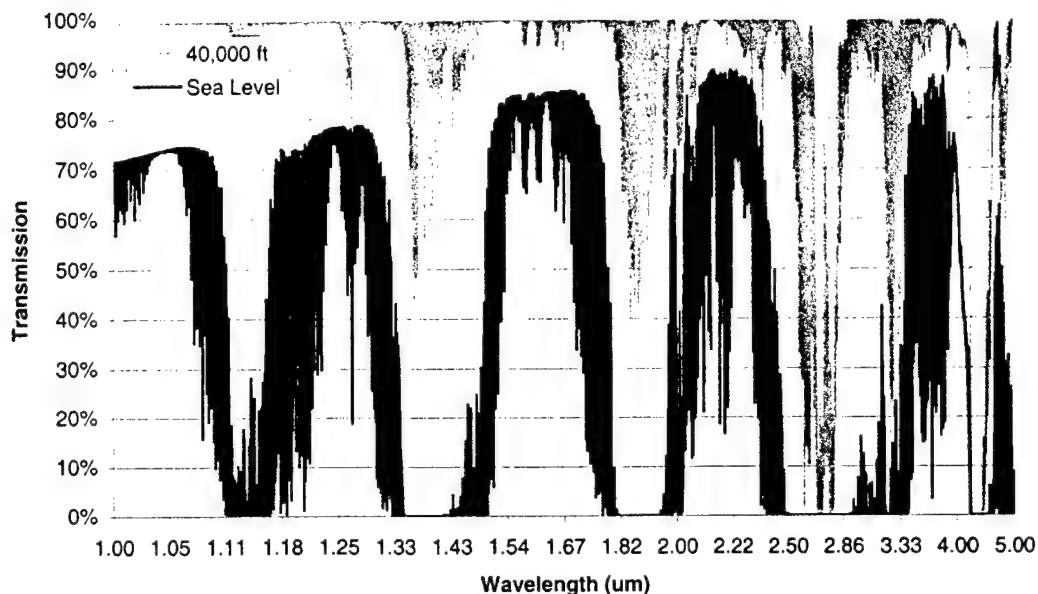
Figure 25 – Atmospheric Transmission Between Target in LEO and Sensor at Varying Altitudes Over Industrial City

(gases, aerosols, clouds, fogs, and rain). HITRAN differs from the other numerical methods in that it is actually a compilation of spectroscopic molecular parameters and not a transmission model. Its resolution is further increased to 0.5 cm^{-1}, making it ideal for laser applications with line-by-line computation. The absorption database is composed of more than 37 molecules with varying spectral line contributions. Beer's law, which models the atmospheric transmission as a function of molecular absorptivity, path length, and concentration, is introduced in this method.

Figure 25 illustrates the atmospheric transmission at 1400 hours on August 18, 1999 in Los Angeles, CA. These curves represent the transmission losses for a sensor at sea level and 40,000 ft ASL, which is near the tropopause or troposphere/stratosphere border. The target for this scenario is in low earth orbit (LEO, approximately 300nm). As mentioned previously, CO_2 concentrations are expected to be at higher levels over a large
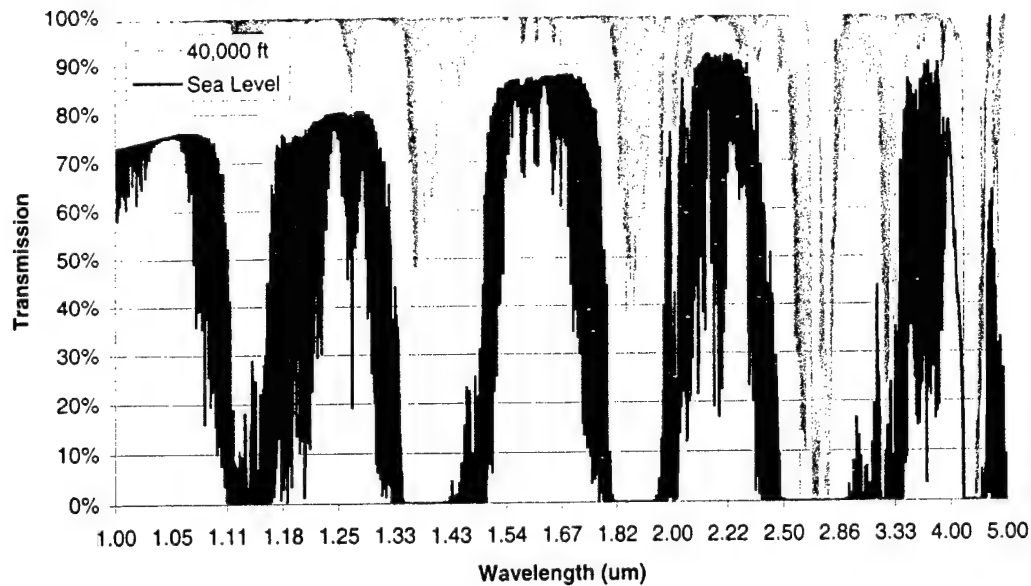
Figure 26 - Atmospheric Transmission Between Target in LEO and Sensor at Varying Altitudes Over Rainforest

industrial city. However, these concentrations tend to dissipate with altitude resulting in decreased CO_2 absorption, as is observed mainly in the narrowing of the absorption band centered at 2.7µm. Also, since temperature decreases (linearly) with increasing altitude through the troposphere, a decrease in H_2O concentrations is expected and is evident in the narrowing of the absorption bands centered at 2.7µm[13] and 3.2µm. The average transmission coefficients for the sea level and 40,000 ft cases are 38.0% and 92.5% respectively.

Figure 26 models the atmospheric transmission for the same date and time as used in Figure 25; however, the location of the sensor and surface projection of the target are now in a rainforest in Brisbane, Australia. The average transmission coefficients for this scenario are 40.7% and 92.7%. These values compared to the previous case fall in line

---

[13] The absorption band centered at 2.7µm is an aggregate of CO_2 and H_2O molecular absorption.

with the theoretical results, since photosynthesis is expected to reduce CO_2 concentrations. Unfortunately the effects of CO_2 absorption cannot be so easily isolated, since an increase in humidity or H_2O vapor content in this region may be affecting the results. The wavelength axis of Figure 25 and Figure 26 appears to be in logarithmic form due to a 1 cm^{-1} spectral resolution causing these linewidths to be functions of wavelength in wavelength space (refer to Equation (26)). Plotting versus wavelength was selected in order to more effectively display the narrower linewidth transmission and absorption windows from $1\mu m$-$2\mu m$. Wavenumber is given by

$$\nu\left[cm^{-1}\right] = \frac{1}{\lambda[cm]} \tag{25}$$

and by

$$\Delta\nu\left[cm^{-1}\right] = \frac{\Delta\lambda[cm]}{\left(\lambda[cm]\right)^2} \tag{26}$$

in differential form, thus producing spectrally varying linewidths in wavelength space.

Both of these figures were generated using a singular software package, which integrates the aforementioned numerical analysis methods, known as PLEXUS (Phillips Laboratory Expert Unified and Software)[14]. PLEXUS is a commercial grade package that provides single point access to these atmospheric codes and celestial optical background codes developed by the Air Force Phillips Laboratory, Geophysics Directorate (now AFRL/VSBM). It was designed to predict and assess the impact of varying radiance

---

[14] A copy of Plexus may be obtained by contacting AFRL/VSBM at (781) 377-3645 or DSN 478-3645

backgrounds on electro-optic systems due to molecular absorption and scattering and aerosol absorption and scattering. In addition to integrating a suite of optical background codes into a single software suite, PLEXUS contains an embedded expert system to facilitate code applications by novice users. The PLEXUS software consists of a code element-based architecture and a graphical user interface (GUI) for accessing the FORTRAN coded atmospheric and celestial background models [4].

After selecting the appropriate parameters within the PLEXUS system, transmission spectra similar to those in Figure 25 and Figure 26 may be integrated into a band selection routine, such as CBand, to prevent bands with reduced transmission from being selected.

Appendix C. Methods of BRDF Measurement

Measurement of material reflectance spectra and calculation of the BRDF can take many forms from an experimental configuration and a post-processing standpoint. The multispectral systems outlined in Section 4.1 and *Active Multispectral Band Selection and Reflectance Measurement System* [19] made certain assumptions regarding the types of materials and their respective properties. The following will address both analytical and empirical methods of calculating the BRDF along with any assumptions made.

C.1 Analytic BRDF Models

In order to reduce the complexity of the BRDF model, many assumptions are typically made, such as: the incident light has uniform energy cross-section and is collimated, all scatter is from the surface and not the bulk of the material, the material is isotropic, and detector apertures (or solid angles) are finite. Equation (2) makes these assumptions

$$\rho' = \frac{\text{differential radiance}}{\text{differential irradiance}} \cong \frac{dP_r/d\Omega_r}{P_i\cos\theta_r} \cong \frac{P_r/\Omega_r}{P_i\cos\theta_r} \tag{27}$$

where P_r is the power reflected by the material, Ω_r is the solid angle subtended from the material surface to the (target) detector aperture or collection optic, P_i is the power incident upon the material surface, and $\cos\theta_r$ is a correction factor that establishes Lambertian reflectors as a baseline (or constant BRDF with respect to reflection angle).

This phenomena is the result of intensity (P_r/Ω_r) falling off with the cosine of the reflected

angle for Lambertian radiators.

C.1.1 Lambertian BRDF

Additional assumptions can be made to further simplify the calculation of the

BRDF. The most simplified form of BRDF assumes the material to be Lambertian. These

surface reflectivities are independent of direction and the results are independent of

incident flux spatial distribution; therefore, only the total incident flux and reflectivity of

the surface is necessary to calculate the BRDF.

$$\rho' = \frac{\rho_o}{\pi} \tag{28}$$

where ρ_o is the reflectivity of the surface and π results from the following relationship for

Lambertian surfaces

$$
\begin{aligned}
M &= \frac{\partial \varphi}{\partial As} = \int_{\Omega d} L \cos \theta_s \, \partial \Omega_d \\
&= \int_0^{2\pi} \partial \varphi \int_0^{\pi/2} L \cos \theta_s \sin \theta \, d\theta \\
&= 2\pi L \frac{1}{2} = \pi L \\
&= \rho_o E
\end{aligned}
\tag{29}
$$

where M is the exitance and is related to the irradiance (E) by a reflectivity factor (ρ_o).

Equation (2) may then be reduced to (Equation (28))

$$\rho' = \frac{\text{differential radiance}}{\text{differential irradiance}} \cong \frac{L_r}{E_i} = \frac{L_r}{\pi L_r / \rho_o} = \frac{\rho_o}{\pi} \qquad (30)$$

A truly Lambertian surface will produce a constant radiance, regardless of illumination or viewing geometry. However, in practice this is not so easily observed, particularly at grazing aspect angles where deviation from Lambert's Law is observed. This leads to the formulation of a BRDF calculation method that will better characterize materials at these grazing angles (refer to Section C.1.3).

C.1.2 Specular BRDF

Another simplified form of the BRDF accounts for purely specular materials. In this case, the BRDF is defined by

$$\begin{aligned}
\rho'(\theta_i,\varphi_i,\theta_r,\varphi_r) &= R(\theta_i)\delta(\Omega_r - \Omega_i) \\
&= R(\theta_i)\frac{\delta(\theta_r - \theta_i)\delta(\varphi_r - \varphi_i + \pi)}{\cos\theta_r \sin\theta_r}
\end{aligned} \qquad (31)$$

where $R(\theta_i)$ is the Fresnel reflectance of the anisotropic surface, Ω_r is the solid angle subtended from the material surface to the detection system, Ω_i is the solid angle subtended from the detection system to the illuminated portion of the material, θ_i and φ_i are the zenith and azimuth incident angles, and θ_r and φ_r are the zenith and azimuth reflection angles

C.1.3 Diffuse Substrate With Glossy Coating BRDF

A more practical scenario combines both diffuse and specular components into one calculation, since many materials exhibit both properties. Equation (32) accounts for materials that are anisotropic and allows for scatter from the bulk as well as the surface [10].

$$\rho'(\theta_i, \phi_i, \theta_r, \phi_r) = R(\theta_i) \frac{\delta(\theta_r - \theta_i)\delta(\phi_r - \phi_i + \pi)}{\cos\theta_r \sin\theta_r} + \dots$$
$$\frac{\rho_o[1 - R(\theta_i)][1 - R(\theta_r)]}{\pi n^2} \tag{32}$$

The first term accounts for the specular surface portion of the BRDF and the second component accounts for the diffuse scatter of the substrate, where ρ_o is the reflectivity of the substrate and n is the refractive index of the dielectric coating. The following is a prime example of the grazing effects of glossy coatings. Suppose a coating has a diffuse reflectance in the LWIR of 0.075 and a refractive index of 1.50. The reflectance (sometimes referred to as directional hemispherical reflectance (DHR)) can be obtained by integrating the BRDF over the desired incident angles (typically defined by the hemisphere). The Lambertian BRDF yields a reflectance of 0.075, while the glossy coating BRDF produces a reflectance of 0.675 for an 86° angle of incidence; this is nearly an order of magnitude increase [10].

C.1.4 Minnaert BRDF

In order to characterize lunar surface reflectance, the Lambertian BRDF (as shown in (30)) is calibrated to model the deviation of reflectance from Lambertian. The *Minnaert BRDF* is given by

$$\rho'\left(\theta_r,\theta_i,k\right)=\frac{\rho_o\left(\cos\theta_r\cos\theta_i\right)^{k-1}}{\pi} \tag{33}$$

where k is the limb darkening parameter [16].

C.1.5 Happke/Lommel-Seeliger BRDF

Another model developed to account for deviations from Lambert's Law and to measures lunar reflectances allows provisions for retroreflection and strong forward and backward scattering. *The Happke/Lommel-Seeliger BRDF* is given by

$$\rho'\left(\theta_r,\phi_r,\theta_i,\phi_i\right)=\frac{\rho_oS\left(2\beta\right)R_f\left(2\beta,g\right)}{\pi\left(\cos\theta_r+\cos\theta_i\right)} \tag{34}$$

where 2β is the angle between the incident and reflected flux directions, S is a scattering function defined separately for forward and reverse directions, g is the ratio of the separation between scatters and the e^{-1} attenuation length, and R_f is the retroreflection (or opposition effect) function [12].

C.1.6 Rough Surface BRDF

Many practical material surfaces are observed to be rough, but not necessarily completely diffuse, thus the *rough surface BRDF* is developed

$$\rho'\left(\theta_r,\phi_r,\theta_i,\phi_i\right)=gR\left(2\beta,n\right)\frac{G\left(\theta_r,\phi_r,\theta_i,\phi_i,n\right)}{\cos\theta_r}e^{-c^2\alpha^2}+\frac{\rho_o\cos\theta_i}{\pi} \tag{35}$$

87

where the first term accounts for rough surface scattering and assumes that the material surface consists of many facets whose surface normals have Gaussian distributions and reflect energy according to Fresnel relations [28]. The model has been verified to produce relatively accurate results below 85° reflection angles for metallic and dielectric materials [10].

C.2 Empirical BRDF Models

This section includes models that incorporate measured data as one or more of the parameters used to fit observed reflectances.

C.2.1 MODIS BRDF

The Moderate Resolution Imaging Spectroradiometer (MODIS) is currently onboard NASA's Earth Observing System (EOS) Terra (polar orbit) satellite platform. MODIS is an across-track wide-field-of-view scanner used to generate a MODIS BRDF/Albedo Product. This system uses a kernel-driven semiempirical Algorithm for Modeling Bidirectional Reflectance Anisotropies of the Land Surface (AMBRALS) method to compute this product. The BRDF and the albedo of each pixel of the global land surface is expected to be modeled at a spatial resolution of 1 km[15].

C.2.2 Robertson-Sanford BRDF

A semiempirical model similar to the *rough surface BRDF* shown in Equation (35)

---

[15] Additional information on this system and its BRDF model can be found at
http://modarch.gsfc.nasa.gov/MODIS/ATBD/atbd_mod09.pdf

is the *Robertson-Sanford BRDF* shown below

$$\rho'(\theta_r,\phi_r,\theta_i,\phi_i) = \frac{\rho_d(\theta_i,\lambda)g(\theta_i)g(\theta_r)}{\pi G^2(b)} + \ldots$$
$$\frac{1}{4\pi}\left[1-\rho_d(\theta_i,\lambda)-\varepsilon(\theta_i,\lambda)\right]\frac{h(\theta_N)}{\cos\theta_r H(\theta_i)} \tag{36}$$

where $\rho_d(\theta_i,\lambda)$ is the diffuse spectral reflectance and $\varepsilon(\theta_i,\lambda)$ is the spectral emissivity related to the spectral reflectance according to Kirchhoff's Law, thus allowing for partial transmission through the material. The grazing angle reflectivity is given by b and the θ_N is the zenith angle of the local surface facet normal [21].

C.2.3 Beard-Maxwell BRDF

The *Beard-Maxwell* model takes empirical BRDF modeling one step further by integrating polarization effects and is given by

$$\rho'(\theta_r,\phi_r,\theta_i,\phi_i) = \frac{R(\beta)\rho_f\cos^2\theta_N}{R(0°)\cos\theta_r\cos\theta_i}\left[\frac{1+\theta_N}{1+\frac{\theta_N}{\Omega}e^{-2\beta/\tau}}\right] + \ldots$$
$$\rho_d + \frac{2\rho_v}{\cos\theta_r+\cos\theta_i} \tag{37}$$

where ρ_d is the diffuse reflectance, ρ_v is the volumetric reflectance, ρ_f is the first surface BRDF, and Ω and τ are shadowing and obscuration parameters used to account for the fact that some surface facets may obscure the line-of-sight between the source or observer and another facet. This model, also similar to the *rough surface BRDF*, assumes that first

89

surface scattering may be modeled by randomly oriented facets and that diffuse scattering can be modeled as the sum of a Lambertian BRDF and the isotropic *Happke/Lommel-Seeliger BRDF*. The first term of this model is the first surface BRDF and includes the polarization dependent Fresnel reflectance (R). The second and third terms are the diffuse and volumetric scattering components.

Bibliography

1. Office of Research and Development (ORD), "Nonconventional Exploitation Factors Data System (NEFDS) Specifications (ORD 258-96 Edition)," 1996.

2. Argus International, Ltd., "Optics & Coatings," Scotts Valley, 1999.

3. Boston, S., "Tunable Range Imaging LADAR System," Final, Rep. A002, Q-Peak, Inc., Bedford, 1999.

4. Calfas, R., "Phillips Laboratory Expert Unified and Software (PLEXUS)," vol. 2000, 1998.

5. Church, E. L. and P. Z. Takacs, "Surface Scattering," in *Handbook of Optics*, vol. I, M. Bass, Ed. New York: McGraw-Hill, Inc., 1995, pp. 7.1-7.12.

6. Cleveland Crystals, "Model IR-1600 Wideband Polarizer," Internet, Cleveland Crystals, Inc., Cleveland, 1997.

7. Csillag, F., L. Paztor, and L. L. Biehl, "Spectral Band Selection for the Characterization of Salinity Status in Soils," in *Remote Sensing Environment*: Elsevier Science Publishing Co., Inc., 1993, pp. 231-241.

8. Dereniak, E. L. and G. D. Boreman, *Infrared Detectors and Systems*. New York: John Wiley & Sons, Inc., 305-311, 1996.

9. Driscoll, W. G. and W. Vaugn, *Handbook of Optics*. New York: McGraw-Hill, Inc., 1978.

10. Erim International, Inc., "Reflectance Modeling Phenomenology and Modeling Tutorial," 1994.

11. Gu, Z. and Z. Lin, "Design Review of a Unique Laser Monostatic Bidirectional Reflectometer," in *Optical Scattering: Applications, Measurement, and Theory II, Proc. The International Society for Optical Engineering*, vol. 1995, pp. 131-137, 1993.

12. Hapke, B., "A Theoretical Photometric Function for the Lunar Surface," *J. Geophys. Res.*, vol. 68, 1963.

13. Hardie, R. C. (a), M. Vaidyanathan (b), and P. McManamon (b), "Spectral Band Selection and Classifier Design for a Multispectral Imaging Laser Radar," (a) Department of Electrical and Computer Engineering, University of Dayton, (b) Air Force Wright Laboratory, Electro-Optics Sensor Branch (WL/AAJT), 1997.

14. Hecht, E., *Optics*, Third ed. Reading, MA: Addison Wesley Longman, Inc., 85-87, 257-276, 1998.

15.   Jelalian, A. V., *Laser Radar Systems*: Artech House, 1992.

16.   Minneart, M., "The Reciprocity Principle in Lunar Photometry," *Astrophysical Journal*, vol. 93, 1941.

17.   Mischler, G., "Rayfront: Lighting Design Knowledge," 1998.

18.   Optoelectronics, P., "J10D Indium Antimonide Infrared Detectors," vol. 1999: PerkinElmer Optoelectronics, 1997.

19.   Rennich, B. D., "Active Multispectral Band Selection and Reflectance Measurement System," Masters Thesis, Department of Physics, Air Force Institute of Technology, Wright-Patterson AFB, 1999.

20.   Sadi, Vukicevic, and M. Torzynski, "Smoothing speckle by three-colour recording," *J.O.S.A.*, 1997.

21.   Sandford, B. and D. Robertson, "Infrared Reflectance Properties of Aircraft Paint (U)," in *IRIS Specialty Group on Targets, Backgrounds, and Discrimination*, 1985.

22.   Satyshur, M. P., "Multispectral Imaging: Band Selection and Performance Predictions," in *IRIS Specialty Group on Targets, Backgrounds, and Discrimination I*, pp. 425-434, 1997.

23.   Schwartz, C. R., M. T. Eismann, J. N. Cederquist, and R. O. Johnson, "Thermal Multispectral Detection of Military Vehicles in Vegetated and Desert Backgrounds," in *Targets and Backgrounds: Characterization and Representation II, Proc. SPIE*, vol. 2742, 1996.

24.   Technical Scientific Services, "Labsphere SRS-99-020 Calibration Data," Rep. 20402-1-1, Labsphere, Sutton, 1997.

25.   Seyrafi, K. and S. A. Hovanessian, *Introduction to Electro-Optical Imaging and Tracking Systems*: Artech House, Inc., 1993.

26.   Stover, J. C., "Optical Scatter: an Overview," in *Optical Scattering: Applications, Measurement, and Theory, Proc. The International Society for Optical Engineering*, vol. 1530, pp. 2-6, 1991.

27.   Surette, M. R., "Optimal Band Selection Based on Hyperspectral Field Measurements," in *IRIS Targets, Backgrounds, and Discrimination, Proc. IRIS*, vol. I, 1995.

28.   Torrance, K. and E. SParrow, "Theory of Off-Specular Reflection From Roughened Surfaces," *Optical Society of America*, vol. 57, 1967.

29.   Vaidyanathan, M., "Tunable 1.3 to 1.5 um Wavelength Target Reflectance Measurement System," Northrop Grumman Corp., Rolling Meadows.

30.   Verdeyen, J. T., *Laser Electronics*, 3rd ed. Englewood Cliffs, NJ: Prentice-Hall, 1995.

Vita

Captain Mark J. Proctor was born in Shreveport, Louisiana on 31 December 1969. After graduating from Parkway High School in 1988, he enlisted and began his Air Force Reserve career through Basic Military Training (BMT) at Lackland AFB, Texas. Following BMT, Mark was assigned to the Keesler Technical Training Center at Keesler AFB, Mississippi for training in avionics, communications, and navigation systems. Mark was later assigned to the 98th Consolidated Air Maintenance Squadron (CAMS) located at Barksdale AFB, Louisiana. After completion of level three maintenance training, Mark entered an undergraduate program in Electrical Engineering at Louisiana Tech University in Ruston, Louisiana. While pursuing his Bachelor's Degree in Electrical Engineering, he enrolled in the university's Air Force Reserve Officers Training Corps (AFROTC) Detachment 305. He completed his degree in 1994 with Magna Cum Laude and Distinguished Graduate honors from Louisiana Tech University and AFROTC respectively. Captain Proctor was commissioned on August 25, 1994, and was assigned to the 452nd Flight Test Squadron, Edwards AFB, California. He worked as a Technical Engineer, Network Administrator, and Advanced Range Instrumentation Aircraft (ARIA) mission commander in support of Department of Defense (DOD), National Aeronautics and Space Administration (NASA), and commercial space launch programs until entering the Air Force Institute of Technology graduate program in August 1998.

1. AGENCY USE ONLY (Leave blank)	2. REPORT DATE March, 2000	3. REPORT TYPE AND DATES COVERED Master's Thesis	

4. TITLE AND SUBTITLE

ACTIVE MULTISPECTRAL BIDIRECTIONAL REFLECTANCE DISTRIBUTION FUNCTION MEASUREMENT SYSTEM

5. FUNDING NUMBERS

6. AUTHOR(S)

Mark J. Proctor, Captain, USAF

7. PERFORMING ORGANIZATION NAMES(S) AND ADDRESS(S)

Air Force Institute of Technology
Graduate School of Engineering and Management (AFIT/EN)
2950 P Street, Building 640
WPAFB OH 45433-7765

8. PERFORMING ORGANIZATION REPORT NUMBER

AFIT/GEO/ENG/00M-02

9. SPONSORING / MONITORING AGENCY NAME(S) AND ADDRESS(ES)

AFRL/SNJ
Attn: Maj Patrick J. Gardner
2241 Avionics Cl, Building 620
WPAFB OH 45433-7765   DSN: 785-4539

10. SPONSORING / MONITORING AGENCY REPORT NUMBER

11. SUPPLEMENTARY NOTES

Maj Eric P. Magee, ENG, DSN: 785- 4604, ext. 4023

12a. DISTRIBUTION / AVAILABILITY STATEMENT

APPROVED FOR PUBLIC RELEASE; DISTRIBUTION UNLIMITED.

12b. DISTRIBUTION CODE

ABSTRACT (Maximum 200 Words)

The purpose of this research involved the development of a 3-dimensional database of material reflectances as a function of target reflection angle and source wavelength. Post-processing of the measured data removes the optical and detection electronics' spectral responses, thus creating a system independent method of characterizing materials of interest. The particular BRDF measurement system implemented in this research is the direct result of a previous attempt that encountered numerous errors. These errors were primarily attributable to nonlinearities, attenuation, and misalignments in the equipment utilized. Considerable effort was expended in order to reduce these anomalies mainly through component replacement, improved measurement techniques, and an extensive system calibration. A comprehensive error analysis is presented for this system along with recommendations for a new configuration, which is expected to further reduce these abnormalities and improve data integrity and collection efficiency.

14. SUBJECT TERMS
bidirectional reflectance distribution function (BRDF), specular, diffuse, Lambertian, isotropic, mid-wave infrared (MWIR), band optimization, band selection, atmospheric absorption

15. NUMBER OF PAGES
108

16. PRICE CODE

17. SECURITY CLASSIFICATION OF REPORT UNCLASSIFIED	18. SECURITY CLASSIFICATION OF THIS PAGE UNCLASSIFIED	19. SECURITY CLASSIFICATION OF ABSTRACT UNCLASSIFIED	20. LIMITATION OF ABSTRACT UL